

# Ultrafast laser-induced black silicon, from micro-nanostructuring, infrared absorption mechanism, to high performance detecting devices

J.-H. Zhao <sup>a</sup>, X.-B. Li <sup>a, \*\*</sup>, Q.-D. Chen <sup>a</sup>, Z.-G. Chen <sup>a</sup>, H.-B. Sun <sup>a, b, \*</sup>

<sup>a</sup> State Key Laboratory of Integrated Optoelectronics, College of Electronic Science and Engineering, Jilin University, 2699 Qianjin Street, Changchun 130012, China

<sup>b</sup> State Key Laboratory of Precision Measurement Technology and Instruments, Department of Precision Instrument, Tsinghua University, Beijing 100084, China

## ARTICLE INFO

### Article history:

Received 29 January 2020

Received in revised form

27 February 2020

Accepted 18 March 2020

Available online 27 March 2020

### Keywords:

Ultrafast laser pulses

Black silicon

Infrared absorption

Hyperdoping

Infrared detection

## ABSTRACT

As the foremost semiconductor, silicon (Si) is the 'lifeblood' of the modern microelectronics and optoelectronics industries. The development of Si infrared (IR) photodetectors is of great significance for Si-based optoelectronic integration and communication. The use of black Si, which can extend the absorption edge of the Si bandgap to IR wavelengths below the bandgap, is a promising strategy to make IR detectors directly integrated on Si wafers for optical communication and detection. To produce black Si, ultrafast laser pulses in an ambient atmosphere or an atmosphere including precursors are used to fabricate periodically arranged micro-nanostructures and induce various defects on Si surfaces. This phenomenon leads to a 'black' color because of a strong absorption from visible light to IR light. In this review, the surface morphology, crystalline structures, hyperdoping, IR absorption properties, and optoelectronic devices of black Si fabricated by ultrafast lasers over the past 20 years are systematically summarized, focusing especially on its most important application for IR photodetectors. Finally, future prospects and strategies for improvement are suggested. It is expected that black Si can be a competitive candidate for IR optoelectronics in the future if thermostable IR absorption, a low concentration of free carriers, and a high photoelectric conversion efficiency of black Si can be achieved.

© 2020 Elsevier Ltd. All rights reserved.

## 1. Introduction

Silicon (Si)-based microelectronic technology has produced remarkable achievements in the past half-century and has greatly promoted the development of information technology. However, as microelectronics are developed at a smaller scale, their quantum features gradually emerge. Moore's law, which has successfully described the development trend of integrated circuits (ICs) over the past 50 years, is also approaching its limit [1]. If Si-based optoelectronic integration using photons and electrons as carriers could be truly realized, then information transmission with an ultralarge capacity, a high transmission rate, and low heat dissipation could be realized. This will have a revolutionary impact on

future communication and computer technologies [2]. As the core unit of Si-based optoelectronic integration, infrared (IR) photodetectors (PDs) with good optical response characteristics have become a current research focus. The goal in this field is to produce high-response, high-speed, low-dark-current, near-IR (NIR) PDs with wavelengths in the communication band of 1.31–1.55  $\mu\text{m}$ . However, because the bandgap of Si is 1.12 eV, Si is transparent to IR light with wavelengths above 1.1  $\mu\text{m}$  [3]. Therefore, crystalline Si (c-Si) cannot be used for the IR detectors required for Si-based optoelectronic integration. At the present stage, IR PDs based on the III–V group semiconductors have been commercially applied because of their high absorption coefficients at 1.31 and 1.55  $\mu\text{m}$ . However, III–V semiconductor materials are expensive, and their manufacturing process is not compatible with the current mature complementary metal–oxide–semiconductor (CMOS) technology, greatly limiting their use in integrated optoelectronics [4,143]. In recent years, micro-nanostructured black silicon (black Si, see the real image in the inset of Fig. 1a), which is obtained by ultrafast

\* Corresponding author.

\*\* Corresponding author.

E-mail addresses: [lixianbin@jlu.edu.cn](mailto:lixianbin@jlu.edu.cn) (X.-B. Li), [hbsun@tsinghua.edu.cn](mailto:hbsun@tsinghua.edu.cn) (H.-B. Sun).

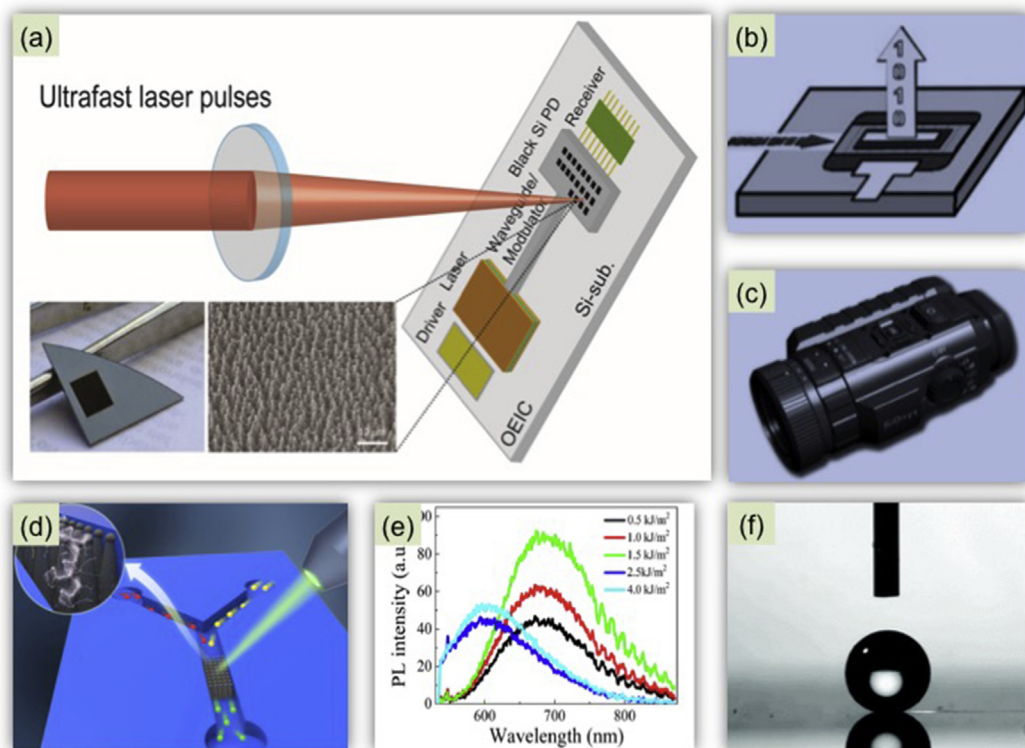


**Fig. 1.** (a) Schematic diagram of the apparatus used for black silicon PD with ultrafast laser pulses, which is integrated on Si-based Optic Electronics Integrated Circuit (OEIC) chip. Inset pictures are the real sample of black silicon [140] and SEM of hyperdoped black silicon with sulfur, respectively. Reproduced with permission. Copyright 2008, SPIE. (b) Near-IR detector application; (c) Night-Vision Camera application [9]; (d) Integrated catalytic reactors and an SERS substrate for sensing [26]. Reproduced with permission. Copyright 2015, Chinese Laser Press. (e) Luminescence device application [29]. Reproduced with permission. Copyright 2011, AIP Publishing LLC. (f) Bionic device application [30]. Reproduced with permission. Copyright 2006, American Chemical Society.

femtosecond (fs) laser irradiation, has exhibited a significant enhancement in the absorption in the NIR region (1.1–2.5  $\mu\text{m}$ ) compared with that of conventional c-Si. Thus, black Si is beginning to be considered as a potential IR detection material [5–8].

The simplified diagram of black Si fabrication by an ultrafast laser is shown in Fig. 1a. A beam of ultrafast laser pulses (with a duration of fs, picosecond [ps], or nanosecond [ns]) is focused by a lens onto a c-Si substrate, which is usually loaded in a vacuum chamber filled with a background gas. To achieve an ablation region with a large area, the vacuum chamber is fixed to a 3D stage in advance so that the position of the laser spot on the Si substrate can be adjusted and controlled by a computer program. After irradiation with ultrafast laser pulses, periodically arranged micro-nanostructures can form on the Si surface (see the scanning electron microscopy (SEM) image of sulfur (S)-doped black Si in the inset of Fig. 1a). The formation of micro-nanostructures on the surface and doping mechanism of black Si can be illustrated by considering the pulsed laser–matter interactions. In the interaction of ultrafast laser pulses with Si material, damage to the Si surface may occur, which is determined by the laser fluence. (1) For laser fluences below the melting threshold, the Si does not melt, and photoexcited carriers relax via carrier–carrier and carrier–phonon scattering. Most of the absorbed energy is transferred to the lattice in the form of heating [141]. (2) When the laser fluence is greater than the melting threshold of Si, the time of energy deposition is close to or shorter than that of heat diffusion. Therefore, heat accumulates before being conducted away from the substrate [32]. Thus, the substrate temperature could be above the melting point of Si, 1,685 K, and a melting layer develops near the surface. Because this thin melting layer remains on top of the cold (room

temperature) lattice, the heat flux away from the molten zone is large, and the resolidification front flows quickly through the Si substrate (possibly exceeding 10 m/s); thus, thermodynamic equilibrium cannot be established at the liquid–solid interface. As a result, dopant atoms present in the melted region will be trapped in the resolidification process above their solid solubility limit. (3) Above the ablation threshold, substantial Si material is removed from the substrate, and ablation damage can be observed. Owing to interference between the incident laser pulse and self-scattering from surface defects, the melt depth of the Si surface periodically varies after application of a single laser pulse. Spontaneously excited waves (capillary waves) in the melting layer freeze in place during resolidification, forming laser-induced periodic surface structures (LIPSS) [142]. Then, subsequent laser pulses are incident on the textured surface, and they preferentially focus on the ‘valleys’ of the structures. (4) A further increase in laser energy will remarkably increase the rate of material removal, leading to ablation of the surface texture. Black Si materials fabricated by ultrafast laser pulse irradiation have many advantages and many attractive applications. First, black Si has excellent absorption from the ultraviolet (UV) to IR regions below the bandgap of c-Si because of its hyperdoping and good geometric light trapping. Therefore, its most important application is in NIR detection, for example, in an IR detector for Si-based optoelectronic integration (Fig. 1a and b) [12–21], an IR night vision camera (Fig. 1c) [9–11], and solar cells [22–25,144]. In addition, laser-etched black Si can be produced in designated areas on Si substrates, such as in the microchannels of a microfluidic chip. Therefore, black Si can also be applied to integrated catalytic reactors and surface-enhanced Raman spectroscopy (SERS) substrates for biosensing and environmental

monitoring (Fig. 1d) [26,145]. In addition, in a laser-irradiated Si layer, black Si can serve as a luminescence device because of the large number of defects in the layer (Fig. 1e) [27–29] and as a bionic device owing to its superhydrophobicity (Fig. 1f) [30].

As an IR photoelectric conversion material, black Si has the following three remarkable properties compared with III–V group semiconductors: (1) Si materials have a lower cost, and insights into various properties of Si have been elucidated. (2) As a detection material, black Si is compatible with the current IC processes, so the application of black Si in future all-Si integrated optoelectronic chips is straightforward. (3) Unlike epitaxial growth technology, ultrafast laser doping has the advantage of area selection, avoiding the need for masking, that is, the ‘cold’ processing characteristics of ultrashort pulsed lasers will not change the physical and chemical properties of non-modified regions. This ensures that other areas in the integrated devices are not affected. Based on the above advantages, black Si materials based on ultrafast laser doping are currently considered to be a key avenue for solving the above problems. However, the following key problems need to be solved before applying black Si materials to NIR detectors: (1) The micro-nanostructures formed by ultrafast laser ablation of Si exhibit a good light trapping effect. However, a surface with rough micro-nanostructures will increase the recombination process of photo-generated carriers, thereby reducing the photoelectric conversion efficiency of the devices. (2) The IR absorption of black Si materials has poor thermal stability, and the IR absorption mechanism still needs to be clarified. (3) The distribution of impurities in the doping layer obtained using a solid dopant lacks uniformity, which will induce a discontinuous junction region.

In this review, we discuss the texturing, hyperdoping, IR absorption, and photovoltaic application of black Si materials fabricated by ultrafast laser pulses. The outline is as follows: First, we discuss the ultrafast-laser-induced surface texture and its dependence on the laser parameters and background atmosphere (Section 2). Second, we focus on the hyperdoping and electronic nature of black Si (Section 3). Third, we discuss the IR absorption properties of black Si (Section 4). Fourth, we discuss typical applications of and progress in PDs based on black Si in detail (Section 5). Finally, a summary and prospects are offered (Section 6).

## 2. Texturing of black Si

### 2.1. Surface morphology of black Si

The surface of *c*-Si is damaged after irradiation with ultrafast laser pulses when the fluence is above the ablation threshold of Si [31,32]. Usually, laser-induced periodically arranged micro/nanostructures are generated on the ablated Si surface [33,34]. The surface morphology after laser irradiation depends on the background environment (gas or liquid) [35–46,148], substrate temperature [47,48], and laser parameters [49–59]. The formed micro-nanostructures are sharper for black Si irradiated under gaseous reactants, such as sulfur hexafluoride (SF<sub>6</sub>), chlorine (Cl<sub>2</sub>), and nitrogen trifluoride (NF<sub>3</sub>), owing to the laser-induced chemical etching effect. This is because chemical reactions between the etchants and Si surfaces can be initiated or enhanced by laser irradiation. The ambient pressure mainly affects the period and depth of the micro-nanostructures. With increasing ambient pressure, the surface morphology changes from nanostructures to ridges, smaller sharper structures, and finally conical microstructures. Further increases in the ambient pressure increase the height and density of the conical microstructures. In addition, a higher substrate temperature can produce a smoother microstructure surface. Sheehy et al. compared the surface morphology of Si irradiated with a train of fs pulses in the presence of different

background gases, such as SF<sub>6</sub>, hydrogen sulfide (H<sub>2</sub>S), hydrogen (H<sub>2</sub>), silane (SiH<sub>4</sub>), and a mixture of argon (Ar) and SF<sub>6</sub> [41,42]. The authors discussed factors that affect the surface morphology created during irradiation and showed that the presence of sulfur (S) in these gases is important for creating sharp micro-nanostructures.

Furthermore, Wen et al. [43] obtained the structural characteristics of Si subjected to fs pulse irradiation in SF<sub>6</sub>, nitrogen (N<sub>2</sub>), air, and vacuum atmospheres. It was found that microcones with defective outer layers formed in the SF<sub>6</sub> atmosphere. The gas atmosphere plays an essential role in forming sharp microcones, and strong laser-assisted chemical etching dominates in laser irradiation processes. The main mechanism of the laser interaction with *c*-Si in N<sub>2</sub>, air, and vacuum is laser ablation because no volatile Si compounds are produced during pulsed laser heating in these background atmospheres. In addition, the Si surface structures obtained by pulsed laser irradiation depend on the ambient pressure. Nivas et al. [44] reported a direct comparison of the results obtained in atmosphere and under high vacuum, highlighting the influence of the ambient pressure on the formation of surface microgrooves with a period larger than the wavelength. Then, the effect of pressures ranging from residual air ambient pressure (10<sup>3</sup> mbar) to high vacuum (10<sup>−4</sup> mbar) on the obtained Si surface structures was proposed. A direct impact of the ambient pressure on the period and depth of the generated ripples, the formation of microgrooves, the shape of the structured area, and the various polarization states was observed [45,46].

The substrate temperature is another important factor controlling the properties of fs-laser-induced surface structures, and the ablation threshold is also a function of temperature for ultrafast-laser-irradiated Si [47]. The morphology of Si surfaces obtained at different temperatures was studied by Deng et al. [48]. Compared to the surface features that form at room temperature (300 K), smoother ripples, microgrooves, and nano/microholes form at higher temperatures (700 K). The results showed that the increased light absorption at an elevated temperature led to a reduction in the surface roughness.

In fact, the micro-nanostructures have specific relationships with the fabrication parameters, including the pulse duration, laser fluence, pulse number, wavelength, polarization, and direction of incident light [49, 50]. During the fabrication process, the pulse number represents the interaction time between the laser and Si, which determines the depth of energy transferred into the inner part of the material, whereas the laser power determines the ablation and volatilization rates of Si [51–53]. With increasing pulse duration, the height of microstructures increases, whereas the density of microstructures decreases. In addition, the surface of black Si is smoother for longer pulse durations. Moreover, the effect of the laser fluence on the surface morphology is multiplex. At a low fluence above the melting threshold, the Si surface is altered in sporadic patches, and the damage that occurs resembles LIPSS. At an increased fluence near the ablation threshold, the surface is covered by a coarsened ripple pattern with a spacing longer than the wavelength of the laser light. The ripples are perpendicular to the polarization of the laser light, and the ripples have a spacing close to the central wavelength of the laser pulses. The density of the structures is larger, whereas the height of the structures is smaller for lasers with shorter wavelengths. At a fluence above the ablation threshold, conical micro/nanostructures develop. With a further increase in the fluence, the height of the microstructures increases, whereas the density of the microstructures decreases. In addition, the direction of microstructure growth is always parallel to the direction of the incident light and is independent of the substrate crystallographic planes. Tull et al. [54] reported on the evolution of micrometer-size cones resulting from irradiation of

single-crystal Si with fs laser pulses in the presence of SF<sub>6</sub> and then proposed a general formation mechanism for the surface spikes. The first pulse caused small defects randomly distributed over the surface (Fig. 2a). Their circular shape suggested that the irradiation formed burst bubbles that were frozen in the places where the melt resolidified. After the second pulse, a distinct ripple pattern appeared (Fig. 2b). The wavelength of the ripple was close to the central wavelength of the incident laser, and the long axis of the ripple was perpendicular to the laser polarization, in agreement with the ripple formation observed in LIPSS. At a high fluence, the interference between the incident beam and light scattered by minor defects on the surface resulted in inhomogeneous energy deposition. Ablation and melt formation occurred at non-uniform depths, creating capillary waves with the same wavelength as the laser. Rapid resolidification subsequently froze the ripple structure in place [54–57]. Ma et al. [58] reported the progressive evolution of Si surface micro-nanostructures with increasing fs laser fluence. Four kinds of micro-nanostructures, including well-defined and clean nanoripples, obscured nanoripples with nanoprotusions and nanoholes, microspikes with nanoholes, and separated microspikes, were obtained by varying the laser fluence (Fig. 3).

Zhu et al. [59] reported a variation in the shape of micro-nanostructures with the polarization direction of the laser beam. With circularly polarized laser irradiation, the shape of the spikes was conical; however, with linearly polarized laser irradiation, the

spikes showed an elliptical conical shape, and the long axes were perpendicular to the polarization direction of the laser beam. The pulse width is another important parameter that affects the surface morphology of black Si. Apart from fs laser pulses, ns laser pulses are also commonly used for fabricating black Si [60–67]. Using an Nd:YAG laser, Sardar et al. [68] reported on the surface morphology of c-Si after applying different numbers of laser pulses in ambient air and SF<sub>6</sub>. The results revealed an increase in the heat-affected zone and melted area of laser-irradiated Si with increasing number of laser pulses. Various surface morphologies, such as LIPSS, craters, microcracks, clusters, cavities, pores, trapped bubbles, nucleation sites, microbumps, redeposited materials, and micro/nanoparticles, can be formed on the surface of irradiated Si [68,69]. Crouch et al. [70] compared the crystallinity of Si micro-nanostructures formed in the presence of SF<sub>6</sub> by fs laser irradiation and by ns laser irradiation. The structures formed with fs pulses were covered with a disordered surface layer less than 1 μm thick, whereas the structures formed with ns pulses exhibited very little disorder (Fig. 4). Similarly, an effect of the laser pulse duration on the morphology of self-organized Si microcones fabricated using 248 nm laser pulses (500 fs, 5 ps, and 15 ns) in an SF<sub>6</sub> atmosphere was presented in the work of Zorba et al. [71].

In addition, fs laser filaments can be used to realize rapid fabrication of black Si. Zhan et al. [72] reported the formation of porous micro-nanostructures on a processed Si surface by this

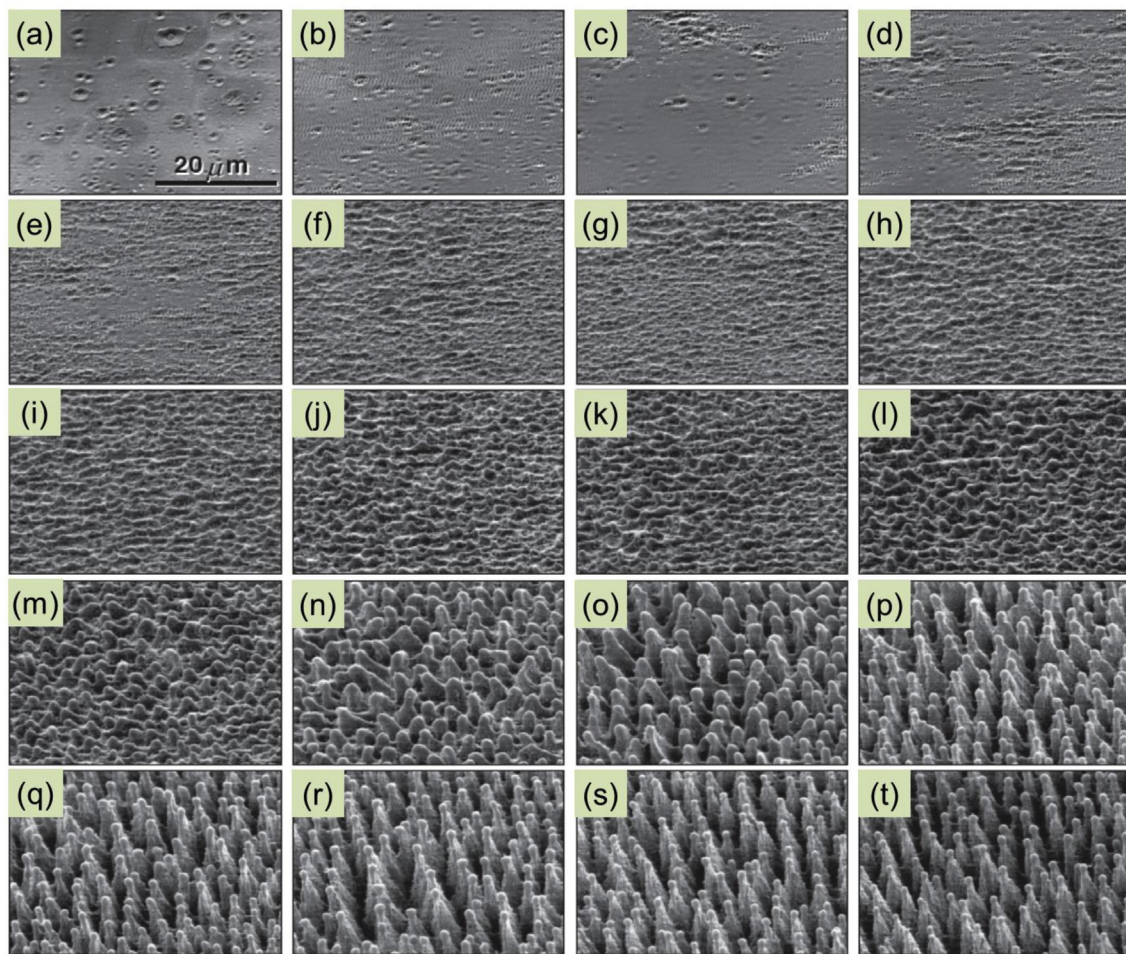


**Fig. 2.** Scanning electron micrographs of a silicon surface after the following number of fs laser pulses: (a) 1, (b) 2, (c) 3, (d) 4, (e) 5, (f) 6, (g) 7, (h) 8, (i) 9, (j) 10, (k) 12, (l) 15, (m) 20, (n) 30, (o) 50, (p) 70, (q) 100, (r) 200, (s) 400, and (t) 600. Each SEM image is taken at a 45° angle to the surface with the same magnification [54]. Reproduced with permission. Copyright 2006, Materials Research Society.

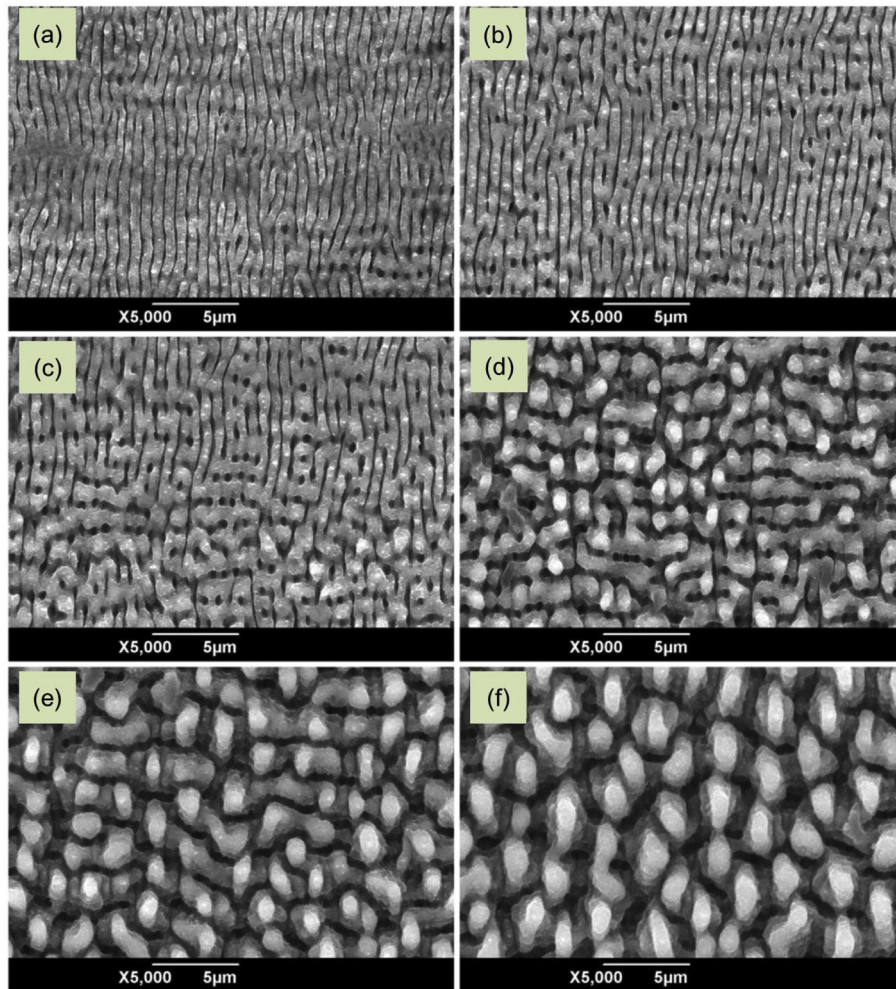


**Fig. 3.** Progressive evolution of silicon surface micro-nanostructures under different laser average fluences. (a) 0.21 J/cm<sup>2</sup>; (b) 0.35 J/cm<sup>2</sup>; (c) 0.48 J/cm<sup>2</sup>; (d) 0.63 J/cm<sup>2</sup>; (e) 0.76 J/cm<sup>2</sup>; and (f) 0.90 J/cm<sup>2</sup> [58]. Reproduced with permission. Copyright 2014, Elsevier.

method. It was found that the air filament can significantly reduce the average number of pulses adopted in a normalized fabrication area and enable remote processing.

## 2.2. Crystal structures of black Si

The crystal structures of black Si layers are mainly affected by the pulse duration. The black Si irradiated by an ns laser is often crystalline. During ultrafast laser irradiation, extreme non-equilibrium processes will result in an Si surface layer of amorphous, polymorphic, and nanocrystalline phases. Sher et al. [73] studied the micro-nanostructure of a sample after laser irradiation with four fs laser pulses at a fluence of 2.5 kJ/m<sup>2</sup>. The center of the laser-irradiated area was crystalline, and the ring with a visible color contrast was amorphous, as demonstrated by the Raman spectra (Fig. 5a). Fig. 5b shows a cross-sectional transmission electron microscopy (TEM) image of the center of the laser-irradiated spot. A fast Fourier transform of the TEM image within the square area in Fig. 5b shows that the center of the sample is single crystalline (inset of Fig. 5b) [73,74].

Gimpel et al. [75] also analyzed the impact of fs laser pulse irradiation on the crystallinity of Si wafers by electron backscatter diffraction (EBSD) measurements. The laser spot was scanned with different overlaps across the sample with one pulse per spot. EBSD

image quality (IQ) maps allow an even more sensitive contrast between the amorphous and crystalline phases to be obtained (Fig. 5c). The low contrast shows that these two rings consist of an amorphous material less than 10 nm thick. The higher contrast within the area of overlap shows that the amorphous layer is thicker than 10 nm in this area. Any other area within the thin amorphous rings is found to be homogeneously white, meaning that the material is crystalline [75,76].

Material ablation during fs laser irradiation of Si generates recoil pressure waves that rise sharply over a few ps and decay over tens of ps. Such ultrafast pressure cycles can drive pressure-induced phase transformations in crystalline Si. Smith et al. [77] investigated the relationship between the parameters of the laser ablation process and the resulting high-pressure phase transformations. They reported direct observations of high-pressure phases and described their formation and distribution. Specifically, the transformation from diamond cubic Si-I to pressure-induced polymorphic crystal structures (amorphous Si, Si-XII, and Si-III) [79] during fs laser irradiation was investigated (Fig. 5d). Amorphous Si, Si-XII, and Si-III were found to form in fs-laser-doped Si regardless of the presence of a gaseous or thin-film dopant precursor. The surface texturing (that occurred during fs laser irradiation) produced inhomogeneous pressure distributions across the surface and caused delayed development of high-pressure Si polymorphs

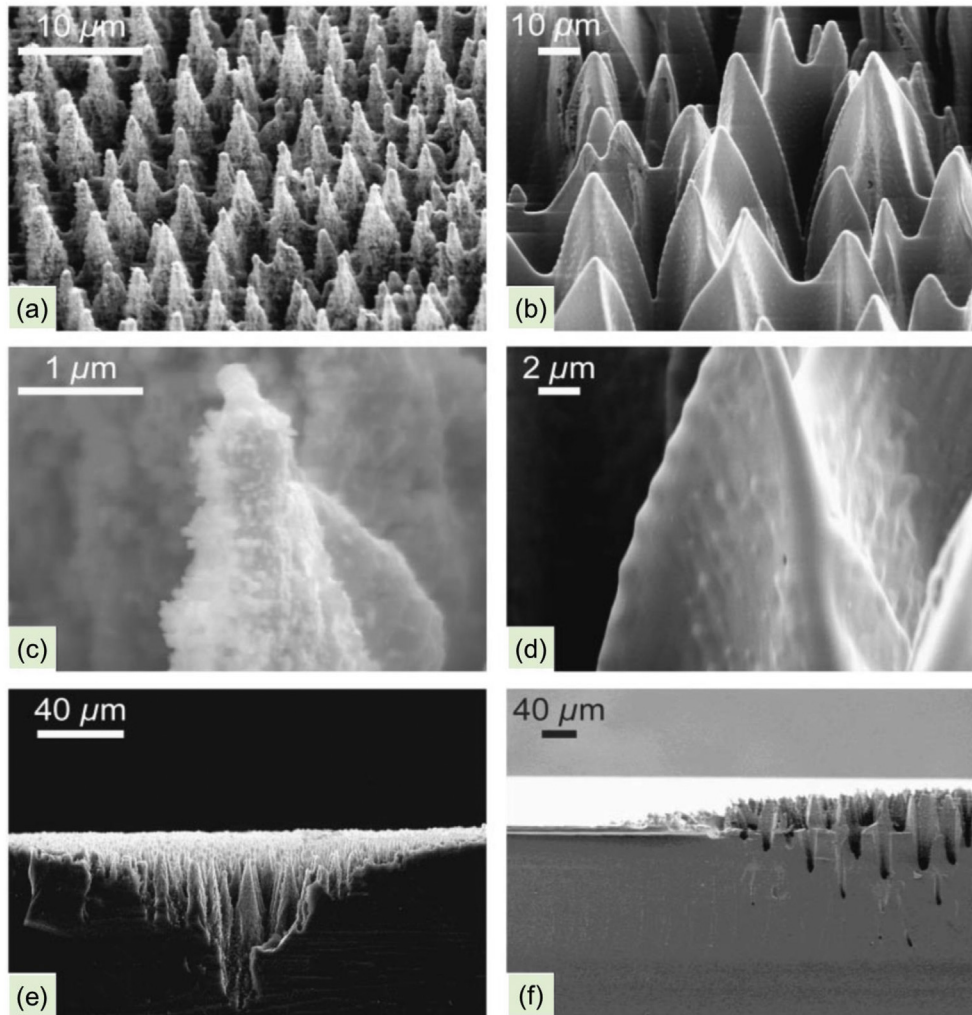


**Fig. 4.** Scanning electron micrographs of laser-micro-nanostructured Si surface formed in  $\text{SF}_6$  [(a), (c), and (e)] with fs laser pulses, and [(b), (d), and (f)] with ns laser pulses. In (a)–(d), the sample is viewed at  $45^\circ$  to the normal; in (e) and (f), the sample is snapped in half and viewed edge-on [70]. Reproduced with permission. Copyright 2004, AIP Publishing LLC.

over many laser pulses. Later, Smith et al. [78] showed that raster scanning of a pulsed laser beam with a Gaussian profile enhances the formation of crystalline pressure-induced Si polymorphs by an order of magnitude compared with stationary pulsed fs laser irradiation. Based on these observations, they identified resolidification-induced stresses as the mechanism responsible for driving subsurface phase transformations during the surface texturing of Si.

### 3. Hyperdoping of black Si

#### 3.1. Sulfur-hyperdoped black Si

$\text{SF}_6$  is used as a popular etching gas to produce micro-nanostructures in Si under laser irradiation, and it was found that c-Si can be hyperdoped with S by fs laser irradiation [73,80–85]. The impurity dose mostly depends on the laser fluence, ambient pressure, and shot number of the pulse. It roughly increases with increasing laser fluence within a certain energy range. At ambient pressures below the critical pressure, the impurity dose is independent of the pressure and the number of laser pulses. At pressures above the critical pressure, the impurity dose increases with both the pressure and the number of laser pulses. Sher et al. [73]

showed the key processes during pulsed laser S hyperdoping (Fig. 6). After laser irradiation, the dopant atoms diffuse from the surface when the Si is molten. The adsorbed dopant molecules can enter the molten Si in one (or a combination) of two ways: (1) the molecules enter relatively slowly (as a flux) over the entire duration of the melting and solidification phases and (2) all the dopant molecules immediately enter on melting. If the dopant concentration in the liquid is higher than the maximum solubility in the solid, then the resolidification dynamics determine the amount of dopant (solute) incorporated (trapped) into the solid phase. Solute trapping depends on the resolidification velocity and the diffusive velocity of the dopant. If the resolidification interface velocity is smaller than the diffusive velocity of the dopant atoms, then excess dopant atoms are ejected into the melt from the solid. If the resolidification velocity is larger than the diffusive velocity, then solute trapping occurs, yielding the dopant concentration [73,81].

Winkler et al. [82] reported the S atom concentration–depth profile for single laser pulse doping (Fig. 7a) under different fluences. S atoms were present as deep as approximately 50 nm in all samples before the secondary-ion mass spectrum (SIMS) signal became heavily influenced by background oxygen (O). S atoms were present at larger depths for lower fluences, but the total S content changed little. Integrating these curves, the total areal S

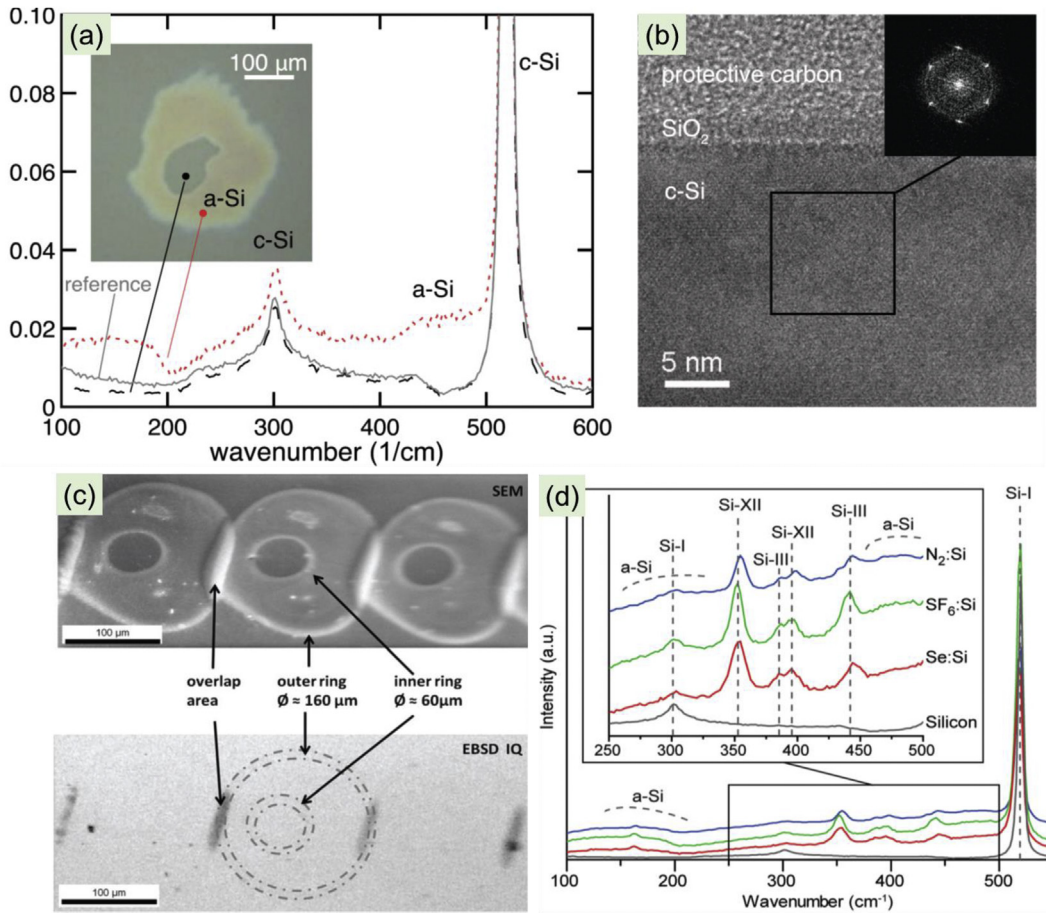


**Fig. 5.** (a) and (b) Micro-nanostructure of a sample hyperdoped at 100-Torr SF<sub>6</sub> with four laser pulses [73]. Reproduced with permission. Copyright 2015, AIP Publishing LLC. (a) Raman spectra taken from three different locations of the sample. The locations are marked in the optical microscope image in the inset. (b) Bright-field TEM image taken from the center of the laser-irradiated spot. Inset: Fast Fourier transform of the TEM image from a hyperdoped area indicated in (b) shows the center of the laser-irradiated region is single crystalline. (c) Reproduced with permission. Copyright 2012, AIP Publishing LLC. Single fs laser pulse lines with a step pitch of  $L = 150 \mu\text{m}$ . Top row: SEM images; bottom row: EBSD IQ maps. Dashed rings mark interface boundary area of the ablation and recrystallization threshold (inner ring) and the modification threshold (outer ring), which both form a low contrast within the EBSD IQ map, meaning this areas to be amorphous with a thickness less than 10 nm [75]. (d) Reproduced with permission. Copyright 2011, AIP Publishing LLC. Stokes Raman spectra of SF<sub>6</sub>:Si, Se:Si, and N<sub>2</sub>:Si, offset to show individual spectra. The rescaled inset highlights the Raman modes corresponding to a-Si, Si-I, Si-III, and Si-XII. The color designation is the same in both plots [77].

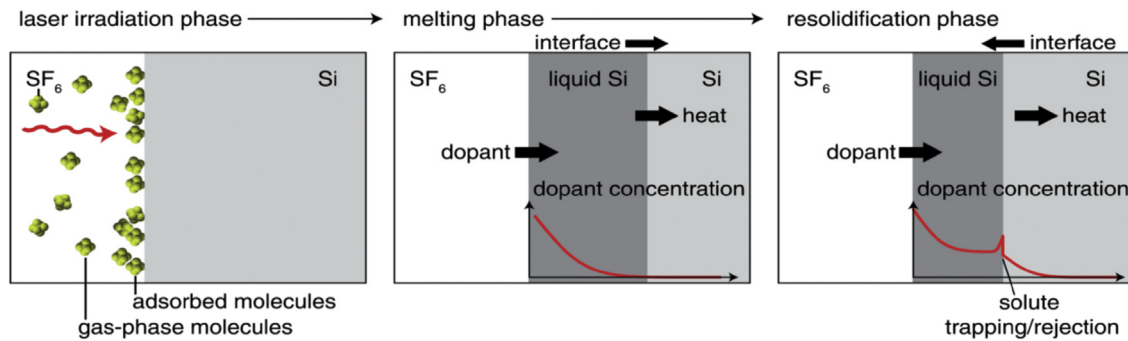


**Fig. 6.** Schematics of the dopant diffusion process during pulsed-laser melting and resolidification. For clarity, SF<sub>6</sub> molecules are only illustrated in the left panel. The arrows show the influx of dopant, heat diffusion, and solid–liquid interface movement. The red curves in the middle and right panels are illustrations of the dopant diffusion profile and effect of solute trapping/rejection [73]. Reproduced with permission. Copyright 2015, AIP Publishing LLC.

dose (number of S atoms per unit area) as a function of fluence is shown in Fig. 7b. Fluences of 3.0 and 3.5 kJ/m<sup>2</sup> yielded a total S dose that was not significantly different from the background, whereas the samples irradiated with fluences of 4 kJ/m<sup>2</sup> and higher exhibited S doses an order of magnitude above the background

level. Among samples with an S dose above the detection limit, the total dose did not vary by more than the measurement resolution [82].

For large-area doping, after laser exposure, the surface retained a mirror-like appearance (Fig. 8a). The laser-melted region, or at

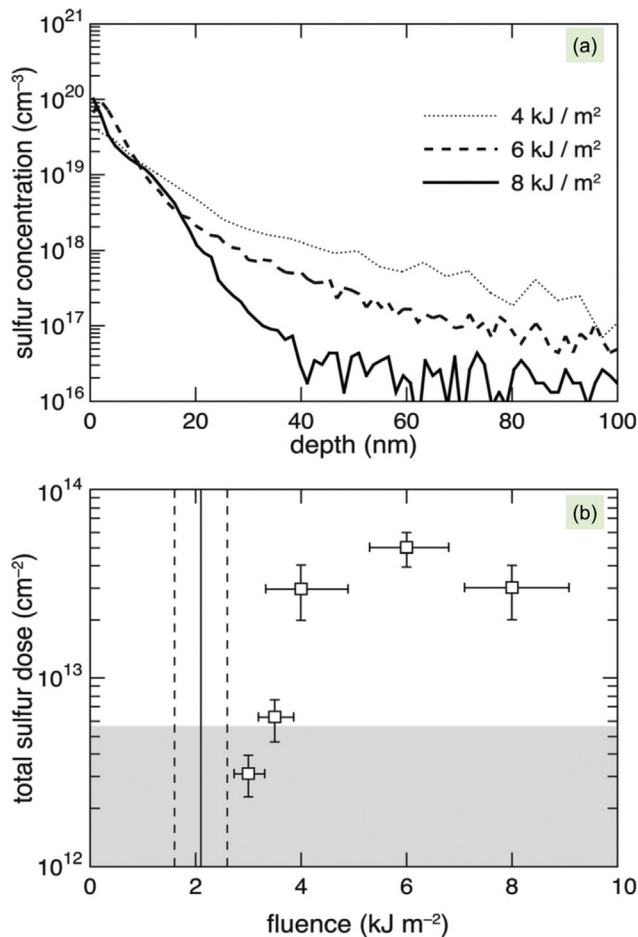


**Fig. 7.** (a) SIMS measurements of fs-laser-doped silicon at several different fluences. (b) The implanted S dose plotted against fluence indicates that S is measurable above the background after irradiation with laser fluences just higher than the measured melting threshold of  $(2.1 \pm 0.5)$  kJ/m<sup>2</sup> (vertical lines). The shaded area indicates the detection limit of the SIMS measurement because of O contamination [82]. Reproduced with permission. Copyright 2012, AIP Publishing LLC.

least its upper portion, resolidified into an amorphous phase (inset of Fig. 8b and d) [82]. The S atom concentration–depth profile is shown in Fig. 8c. The concentration of S atoms near the surface was at least  $6 \times 10^{19}$  cm<sup>-3</sup> and remained above the solid solubility limit ( $10^{16}$  cm<sup>-3</sup>) of c-Si up to a distance of  $90 \pm 14$  nm from the surface, where it fell below the measurement limit because of oxygen contamination. The total areal S dose was  $(2.8 \pm 0.2) \times 10^{14}$  cm<sup>-2</sup>. Electrical measurements revealed that less than 1% of S was electrically active as a donor [82,83].

The S concentration also depends on the pressure of the background atmosphere and laser pulse number. Sher et al. [73] investigated the dependence of the S concentration on the SF<sub>6</sub> pressure and the number of laser pulses. Fig. 9a shows the S concentration profiles of samples irradiated at 0.5 Torr. At this pressure, the dopants were incorporated deeper into the Si with each additional laser pulse, but the total S dose (area under the concentration curve) remained constant. At a higher pressure of 100 Torr, on the other hand, both the surface concentration and the depth of the dopant distribution increased with the number of laser pulses (Fig. 9b). In all profiles, the S concentration exceeded its maximum solubility in solid Si [73]. Fig. 9c shows samples irradiated by four laser pulses across the entire range of pressures investigated. For samples hyperdoped at or below 1 Torr, the concentration profiles

were identical. For pressures greater than or equal to 10 Torr, the S concentration at the surface increased with pressure. Regardless of the SF<sub>6</sub> pressure, the dopant incorporation depth was the same. The total incorporated S is shown in Fig. 9d. The figure shows two pressure regimes, with a transition at a critical pressure ( $P_{crit}$ ) between 1 and 10 Torr. At SF<sub>6</sub> pressures below the critical pressure, the S dose was independent of the pressure and the number of laser pulses. At pressures above the critical pressure, the S dose increased with both the pressure and the number of laser pulses [73,84].

A microscopic analysis of c-Si doped by fs laser pulse irradiation in an SF<sub>6</sub> atmosphere was carried out by Sickel et al. [85]. A cross-section analysis of S-doped samples is provided in Fig. 10, showing SEM (a) and electron-beam-induced current (EBIC, b) maps of the same regions. The position of the maximum EBIC was obtained as the depth of the p–n junction (the dotted line), independent of the surface roughness. From the virtual absence of an EBIC signal in the crest regions, it can be estimated that the effective diffusion length of the excess carrier should be less than 500 nm. The very high defect density (such as dislocations, dislocation loops, and cavity-like defects) below the crests basically quenched the EBIC signal because of strong excess carrier recombination (Fig. 10b) [85].

### 3.2. Other hyperdoping elements of black Si

In addition to S hyperdoping by fs lasers, other elements can also be hyperdoped into an Si surface by laser doping. Similar to S doping, nitrogen (N) has also been doped into Si by the fs laser doping technique in a NF<sub>3</sub> or N<sub>2</sub> atmosphere, and the concentration of the doped N atom was several orders of magnitude above its solid solubility in Si crystals. The average N atom concentration in the uppermost 50 nm was approximately  $0.5 \pm 0.2$  at.% [86,87].

S-doped and N-doped Si samples have been demonstrated using pulsed laser irradiation in the presence of SF<sub>6</sub> and NF<sub>3</sub> (or N<sub>2</sub>) gases, respectively. To further advance the hyperdoping concept, the deposition of a powder or a thin film of a dopant on the Si substrate would enable the introduction of dopants that are unavailable, highly volatile, or toxic in the gas phase and thus open up ultrafast laser doping to a wider range of elements [88]. For example, the deposition of a chalcogen thin film [such as selenium (Se) or tellurium (Te)] on an Si substrate followed by fs laser irradiation has been shown to result in an increase in the sub-bandgap absorption. Different from the case using a gaseous dopant precursor, pulsed laser doping of a thin film produced discontinuous regions of doped material isolated within polycrystalline surface peaks. The differences in the surface texturing processes observed during the gas and thin-film fs laser doping processes raised questions about the possible effects of Se impurities. Thermodynamically, the presence of impurities in Si affects the melting temperature and, in turn, the volume of amorphous material generated. The effects of a thin-film dopant precursor (Se or Si/Se bilayer films) on dopant incorporation have been studied. A sample prepared using an Se thin-film precursor (Se:Si) contained micrometer-scale volumes of polycrystalline Si within each surface peak, the entire polycrystalline region was Se-rich, and the thin-film-doped Se:Si surface was discontinuous [88,89]. However, a more uniform dopant incorporation can be achieved by moving to sufficiently low fluences, in the range of 1.3–1.4 kJ/m<sup>2</sup> under these irradiation conditions. After 10 pulses, a layer of Se dopant precursor remained on the surface, and after 100 pulses, a continuous Se-rich crystalline layer formed in parallel with LIPSS (Fig. 10c) [90]. A TEM micrograph of the microstructure after 100 laser pulses at 1.4 kJ/m<sup>2</sup> was shown in Fig. 10d. At fluences  $\leq 1.4$  kJ/m<sup>2</sup> a continuous doped layer across the surface of the ripples was observed, as confirmed by energy dispersive X-ray (EDX) spectroscopy. Annealing produced significant Se segregation into the grain boundaries, Se precipitates and

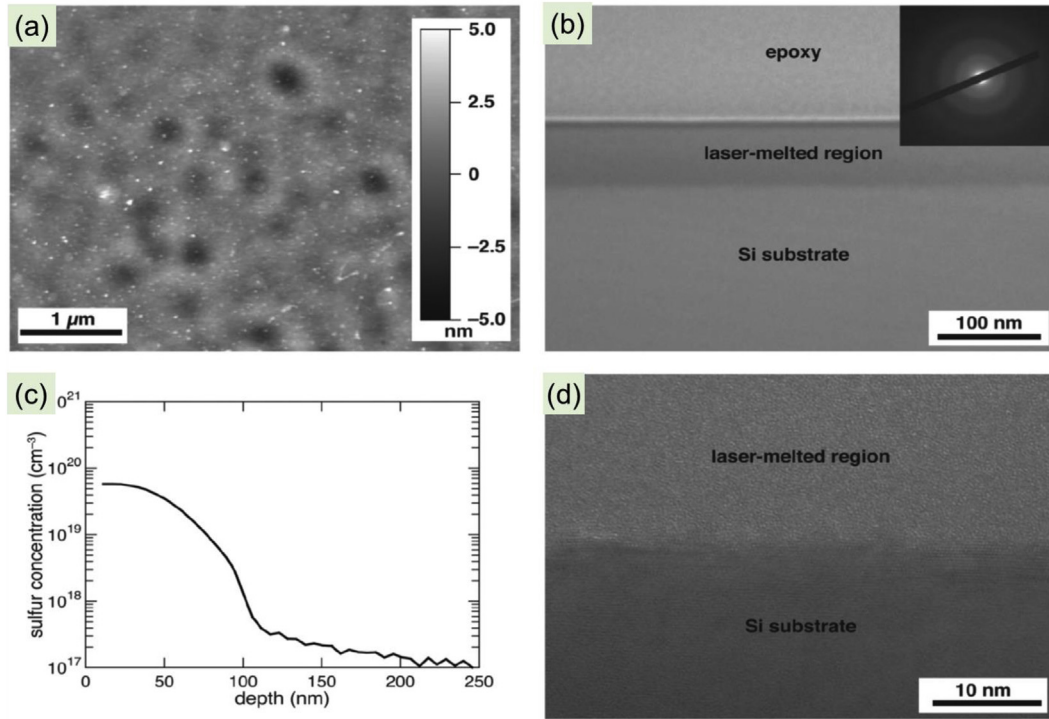


**Fig. 8.** Chemical and structural characterization of laser-hyperdoped silicon. (a) Atomic force microscope image of the laser-irradiated surface. (b) Brightfield (BF) TEM image showing an amorphous silicon layer extending  $66 \pm 7$  nm from the surface, with the crystalline substrate underneath. Inset shows selected area diffraction of the laser-melted region. (c) Depth profile of the S concentration. The measured concentration exceeds the solid solubility limit of S in crystalline silicon at depths not greater than  $90 \pm 14$  nm. (d) High-magnification TEM image revealing the amorphous and crystalline interference patterns of the surface region and substrate, respectively [82]. Reproduced with permission. Copyright 2012, AIP Publishing LLC.

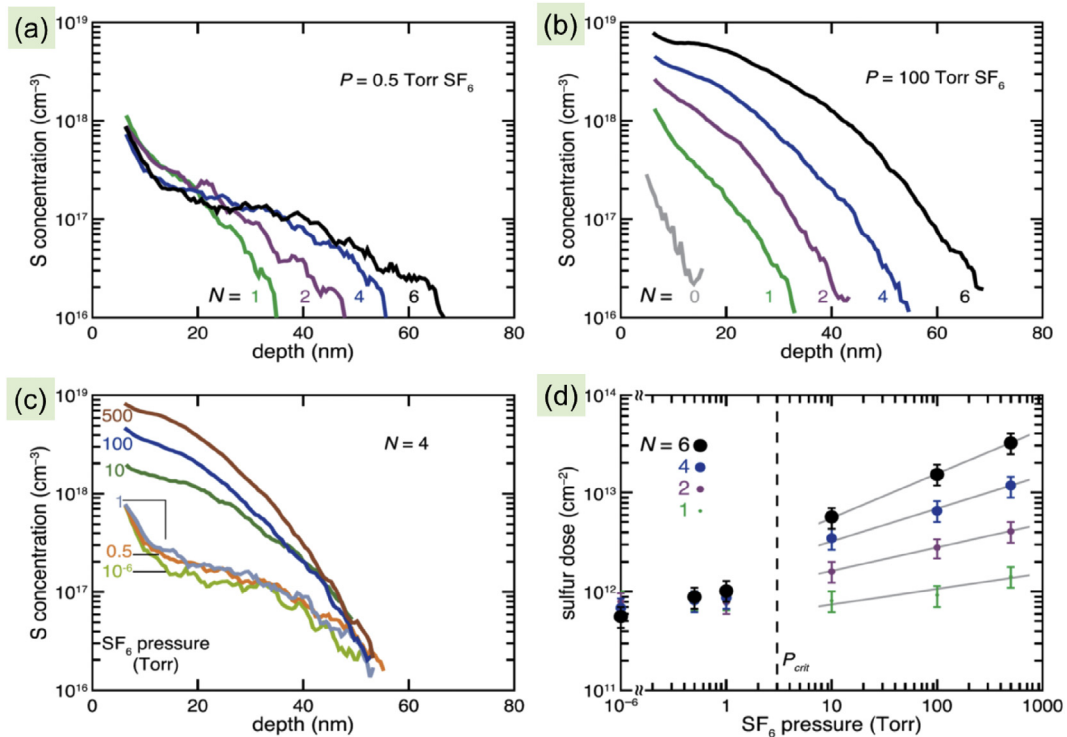


**Fig. 9.** S concentration profiles of samples hyperdoped at (a) 0.5 Torr and (b) 100 Torr. (c) S concentration profiles of samples irradiated by four laser pulses at different pressures. (d) Total incorporated S dose as a function of  $\text{SF}_6$  pressure,  $P$ , and number of laser pulses,  $N$  [73]. Reproduced with permission. Copyright 2015, AIP Publishing LLC.

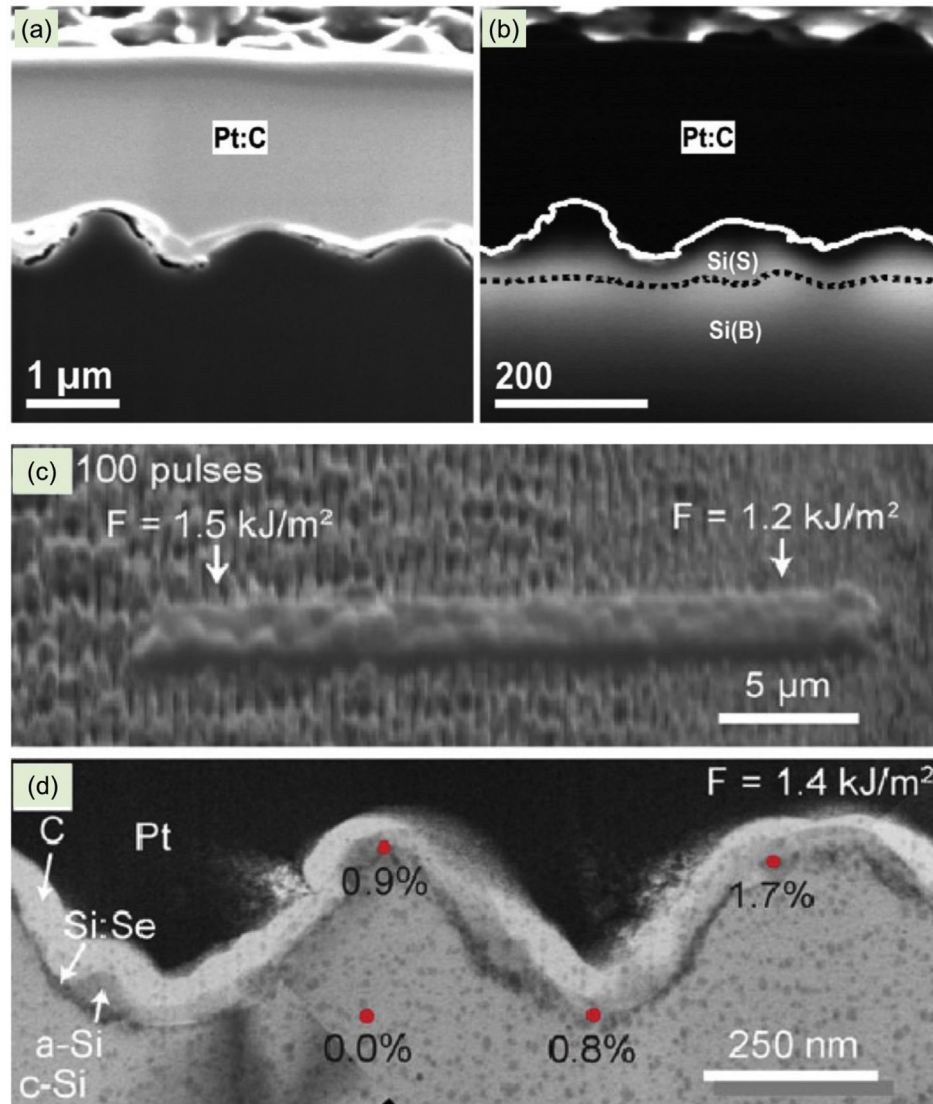


**Fig. 10.** (a) and (b) show focused ion beam prepared cross-section after S hyperdoping [85]. Reproduced with permission. Copyright 2017, WILEY-VCH Verlag GmbH & Co. KGaA, Weinheim. (a) Surface topography. (b) EBIC map of the same region showing the strongly reduced signal in the crest regions. Part (b) also contains the position of the p–n junction as determined from the maximum EBIC signal (black dotted line) and the approximate surface position (white solid line) determined using an edge-finding algorithm on the SEM image shown in (a). (c) and (d) show SEM and TEM images of Se hyperdoped Si, respectively [90]. Reproduced with permission. Copyright 2013, Springer-Verlag Berlin Heidelberg. (c) SEM image of low-fluence region (1.2–1.5 kJ/m<sup>2</sup>) irradiated with 100 laser pulses. (d) BF-TEM image of surface irradiated with 100 pulses at 1.4 kJ/m<sup>2</sup> shows laser-induced periodic surface structures have a continuous crystalline surface layer. EDX point scans indicate Se composition in surface layer of around 1%. For clarity, the crystalline substrate (c-Si), hyperdoped silicon (Si:Se), amorphous silicon (a-Si), and protective coatings (Carbon-C, Platinum-Pt) are indicated.

voids in the Se-rich material. A large number of precipitates formed during the annealing process [91].

In addition to Se doping, pulsed laser phosphorus (P)-hyperdoped Si with a concentration of  $10^{21}$  cm<sup>-3</sup> and pulsed laser gold (Au)-hyperdoped Si with a concentration of  $10^{19}$  cm<sup>-3</sup> (Fig. 11a) were obtained using P paper and Au thin-film precursors, respectively [92–94]. Ultrafast laser doping is not limited to only one kind of impurity. By fs laser irradiation in a gas mixture of NF<sub>3</sub> and SF<sub>6</sub> or N<sub>2</sub> and SF<sub>6</sub>, researchers obtained cohyperdoped samples [95,96]. In the irradiation process, both S and N were incorporated into the surface layer at concentrations several orders of magnitude higher than their solid solubility in Si crystals (Fig. 11b) [95]. Other codoped Si materials, such as those with (S, Se) codoping or (S, O) codoping, have also been investigated [97,98].

## 4. IR absorption of black Si

### 4.1. IR absorption of black Si and its stability

A special feature of pulsed-laser-doped Si is that its absorption can be extended to the IR region ( $>1.1$  μm). Typically, the IR absorption of black Si is determined by the dopant elements, ambient pressure, laser fluence, number of pulses, and annealing temperature. Doping that can introduce deep levels or bands into the bandgap of Si is useful. For gaseous dopants, the IR absorption approximately increases with increasing ambient pressure, laser fluence, and pulse shot number, whereas it decreases with increasing annealing temperature. Wu et al. [6] first reported an increase in the absorption of Si to approximately 90% from the near-

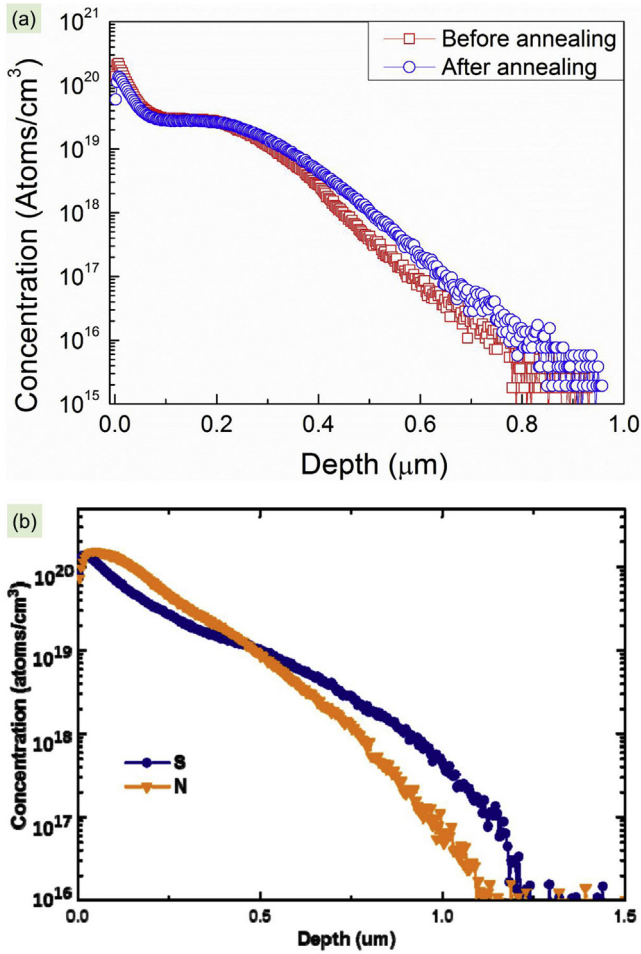


**Fig. 11.** (a) SIMS depth profiles of Au in fs-laser-irradiated Si and corresponding thermal annealed sample (823 K and 30 min in Ar atmosphere) [94]. Reproduced with permission. Copyright 2017, IEEE. (b) SIMS measurements of S and N on the surface layer of the sample prepared in a gas mixture of  $\text{NF}_3$  and  $\text{SF}_6$  with a laser fluence of  $8.6 \text{ kJ/m}^2$  [95]. Reproduced with permission. Copyright 2016, Optical Society of America.

UV (0.25  $\mu\text{m}$ ) to the NIR (2.5  $\mu\text{m}$ ) after fs laser etching in an  $\text{SF}_6$  atmosphere (Fig. 12a). The remarkable absorption most likely arises from the high density of impurities and structural defects in the Si lattices [6,99,100]. The absorption (at 1.2 and 2.5  $\mu\text{m}$ ) of micro-structured Si strongly increases with three fabrication parameters: the number of pulses, the laser fluence, and the  $\text{SF}_6$  pressure [101]. Liu et al. [102] prepared a micro-structured Si surface using ps laser pulses in  $\text{SF}_6$ . The samples exhibited high optical absorption over a wide wavelength range between 0.3 and 2.7  $\mu\text{m}$ . The high IR absorption of the surface-structured samples increased with increasing laser fluence. The IR absorption can be further enhanced by the deposition of a metal film [103,104].

In addition to S doping, other chalcogen doping strategies, such as Se and Te hyperdoping, also led to strong broadband sub-bandgap absorption of Si (Fig. 12b) [105–107]. Sher et al. [107] measured absorption to wavelengths up to 14  $\mu\text{m}$  using Fourier transform IR (FTIR) spectroscopy and studied S-, Se-, and Te-hyperdoped Si before and after annealing. They found that the absorption in the samples can be extended to wavelengths as far as 6  $\mu\text{m}$ . After annealing, the absorption spectrum exhibited a feature consistent with free carrier absorption. The shapes of the absorption curves (low-energy cutoff) were sensitive to the surface

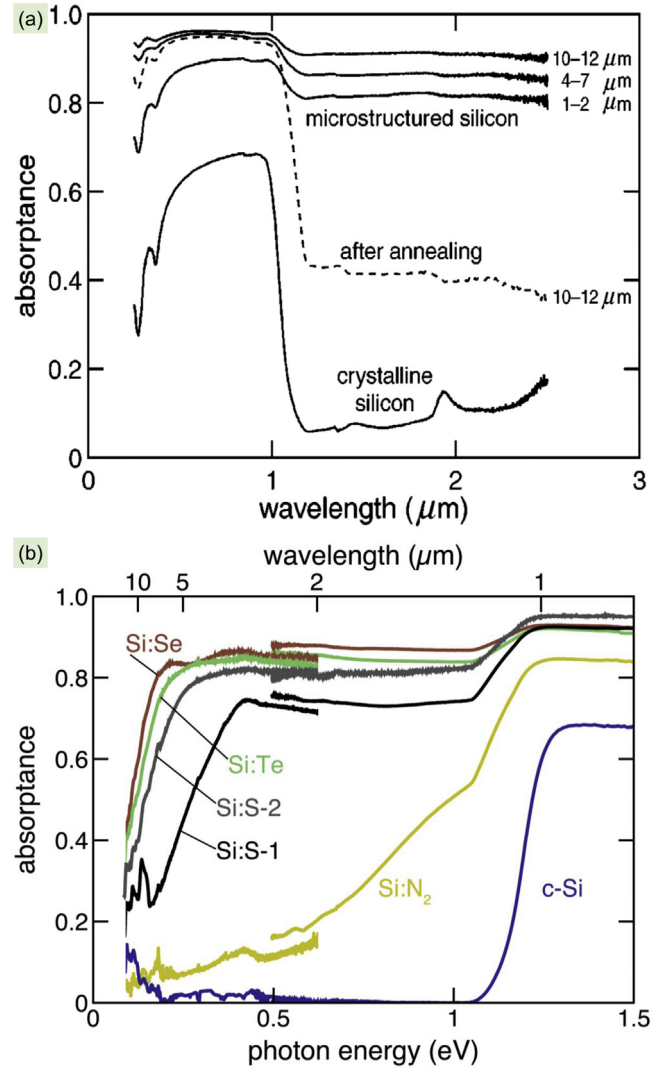


**Fig. 12.** (a) Absorbance of micro-nanostructured silicon surfaces and unstructured silicon substrate [6]. Reproduced with permission. Copyright 2001, AIP Publishing LLC. (b) Absorbance of chalcogen-hyperdoped silicon. Data for a control sample ( $\text{Si:N}_2$ ) and the silicon substrate (c-Si) are also plotted for comparison. Data from 0.09 to 0.62 eV was collected using an FTIR spectrometer and data from 0.5 to 1.5 eV was collected using a UV–VIS–NIR spectrophotometer. The mismatch between the data from two instruments at 0.5 eV is about 3% [107]. Reproduced with permission. Copyright 2013, AIP Publishing LLC.

morphology as a result of the laser irradiation enhancing antireflection and light trapping.

In addition, other micro-nanostructured Si materials fabricated by fs laser irradiation in different gas atmospheres, such as  $\text{Cl}_2$ , air,  $\text{N}_2$ ,  $\text{NF}_3$ , and vacuum, also showed enhanced absorption behavior [7,108–113]. However, the IR absorption of these micro-nanostructured Si materials in the 1.2–2.5  $\mu\text{m}$  wavelength range was lower than that of Si fabricated in  $\text{SF}_6$ . Particularly, greatly enhanced light absorption was observed in the wavelength range from 0.3 to 16.7  $\mu\text{m}$  for micro-nanostructured Si fabricated in  $\text{N}_2$  ambient [109]. The light absorption was up to 95% over the wavelength range of 0.3–1.1  $\mu\text{m}$  and as high as 75% or greater in the wavelength range of 8.8–13.3  $\mu\text{m}$ , although it was down to approximately 30% in the wavelength range of 2–7  $\mu\text{m}$  [109,110]. Similarly, Si subjected to fs laser irradiation in the presence of  $\text{NF}_3$  exhibited a high absorption up to 0.8 and in the mid-IR wavelength range of 3–16  $\mu\text{m}$ . In addition, the absorption of the sample

remained almost unchanged after the annealing process [111–113]. The N doping process (such as that using  $N_2$ ,  $NF_3$ , or N-containing gas of  $SF_6/NF_3$  or  $SF_6/N_2$ ) can improve the crystallinity in the doped layer because the doped N atoms can repair defects in Si lattices.

Thermal annealing causes deactivation of the sub-bandgap optical absorption, although annealing-insensitive black Si has been obtained using Si substrates with high doping [114,115]. In Crouch's work [101], annealing at temperatures below 575 K had little effect on the absorption of Si. Annealing between 575 and 875 K lowered the below-bandgap absorption; the higher the temperature was, the greater the decrease in the absorption. Increasing the annealing

temperature to above 875 K did not produce an additional change (Fig. 13a) [101,116]. In addition, a decrease in the IR absorption ( $\lambda = 1.1\text{--}2.4\ \mu\text{m}$ ) has also been observed in S-hyperdoped black Si fabricated using an Nd:YAG ns pulsed laser [117].

Different from thermal annealing, laser annealing had little effect on the sub-bandgap absorption of micro-nanostructured Si. To obtain high crystallinity and remove pressure-induced phases in hyperdoped black Si, ns laser annealing was adopted by Franta et al. [118] to show that high sub-bandgap optical absorption of Si could be maintained. Furthermore, it was shown that ns laser annealing can reactivate the sub-bandgap absorption of hyperdoped black Si after the deactivation induced by the thermal annealing process (Fig. 13b). Moreover, thermal annealing and ns laser annealing can be combined in sequence to fabricate hyperdoped black Si that shows high crystallinity, high above-bandgap and sub-bandgap absorption, and a rectifying electrical homojunction. Thus, the combination of the thermal annealing (equilibrium processing) and ns laser annealing (non-equilibrium processing) techniques could be a useful approach for controlling the properties of non-equilibrium black Si materials in general [118,119].

#### 4.2. IR absorption mechanism of black Si

The supersaturated concentration of dopant atoms and point defects in black Si give rise to near-unity absorption of below-bandgap light. The below-bandgap absorption of hyperdoped Si suggests an altered band structure, which can be attributed to the formation of impurity bands because of the presence of high concentrations of impurities at the surface of the sample [120–122]. Chalcogen doping could create deep levels in the bandgap of Si, where the deepest-lying state was 0.614, 0.593, and 0.411 eV below the conduction band edge for the dopants of S, Se, and Te, respectively [121]. A supersaturated solution of chalcogen dopants in an Si lattice created one or more impurity bands around the discrete states, observed in the thermal doping of c-Si, and these impurity bands were responsible for the absorption of below-bandgap radiation. In addition, various combinations of S atoms and point defects in the Si lattice—such as vacancies, dangling bonds, and floating bonds—resulted in several midgap states. Furthermore, deep-level transient spectroscopy (DLTS) of S-doped black Si was performed by Baumann et al. [120] (Fig. 14a). Possible S energy states in the Si bandgap were shown in Fig. 14b [149]. From the DLTS spectrum, the deep level related to the S defect state in black Si was changed by the thermal annealing process (800 °C for 30 min).

For the decrease in the below-bandgap absorption of the annealed sample, the most likely explanation was that laser micro-nanostructuring caused S impurities to be trapped in the Si lattice in the form of an optically active state, and annealing caused bond rearrangement within the Si matrix that rendered the S impurities optically inactive. It is also possible that optically inactive precipitates or S–Si complexes formed on annealing [101].

In addition, the investigations by Tull et al. [8] showed that the deactivation of IR absorption after thermal annealing was likely caused by dopant diffusion. Diffusion of the dopants or point defects out of the grains to the grain boundaries reduced the number of impurity levels in the bandgap and thus reduced the IR absorption (Fig. 14c). The authors observed that the characteristic diffusion length led to a reduction in the IR absorption [8,121]. In addition, the research of Haberfehlner et al. [91] suggested that diffusion-limited segregation was responsible for the optical deactivation of Se with annealing.

Moreover, the effect of the chemical states and electronic-atomic structures on the sub-bandgap absorption of S-hyperdoped Si has been extensively studied using synchrotron-based

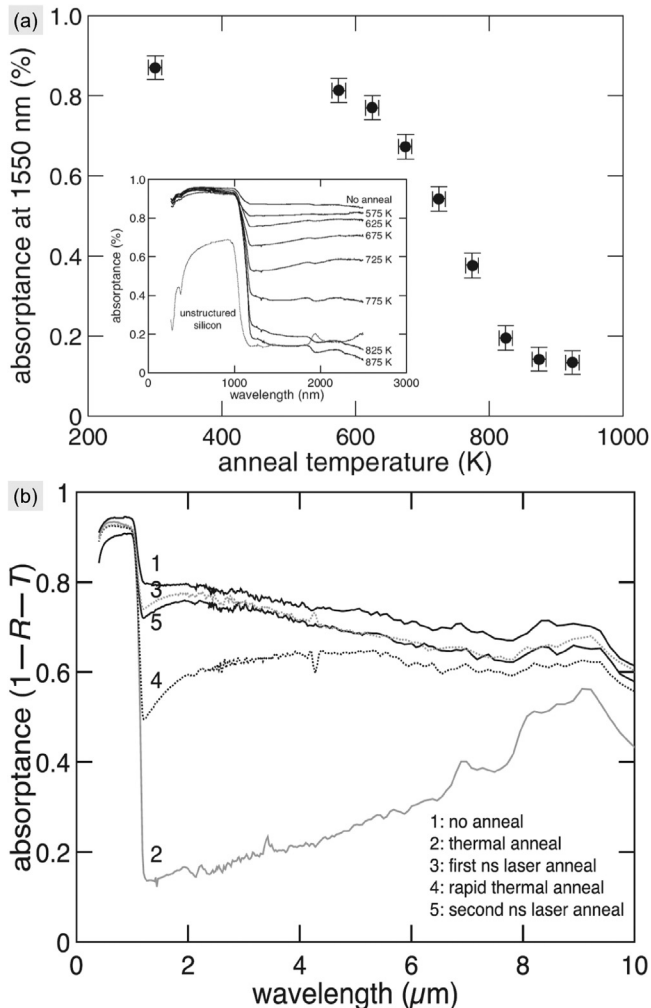


**Fig. 13.** (a) Effect of annealing temperature on absorbance at 1.55  $\mu\text{m}$  of micro-nanostructured silicon surfaces. The data point at room temperature (300 K) corresponds to a sample that was not annealed. All samples were made with 500 laser pulses and  $8\ \text{kJ}/\text{m}^2$  laser fluence in 0.67 bar  $SF_6$ , and were annealed for 30 min. Inset: Wavelength dependence of absorbance for the samples shown in Fig. 4 and for the unstructured silicon substrate. Reproduced with permission from Ref. [101]. Reproduced with permission. Copyright 2004, Springer-Verlag. (b) The effects of thermal and ns laser annealing in sequence on the optical absorbance. (1) Fs-laser-fabricated hyperdoped black silicon exhibits high above-bandgap and sub-bandgap optical absorbance. (2) Thermal annealing (700 °C, 30 min) crystallizes the hyperdoped black silicon but deactivates its sub-bandgap optical absorbance. (3) Ns-laser annealing (here, with a fluence of  $1.1\ \text{J}/\text{cm}^2$ ) maintains the high crystallinity while reactivating the sub-bandgap optical absorbance near to its original level. (4) Rapid thermal annealing (500 °C, 30 s) after depositing electrodes again deactivates (partially) the sub-bandgap optical absorbance. (5) Ns-laser annealing again reactivates the sub-bandgap optical absorbance near to its original level. The final hyperdoped black silicon diodes are highly crystalline, highly optically absorbing, and electrically rectifying [118]. Reproduced with permission. Copyright 2015, AIP Publishing LLC.

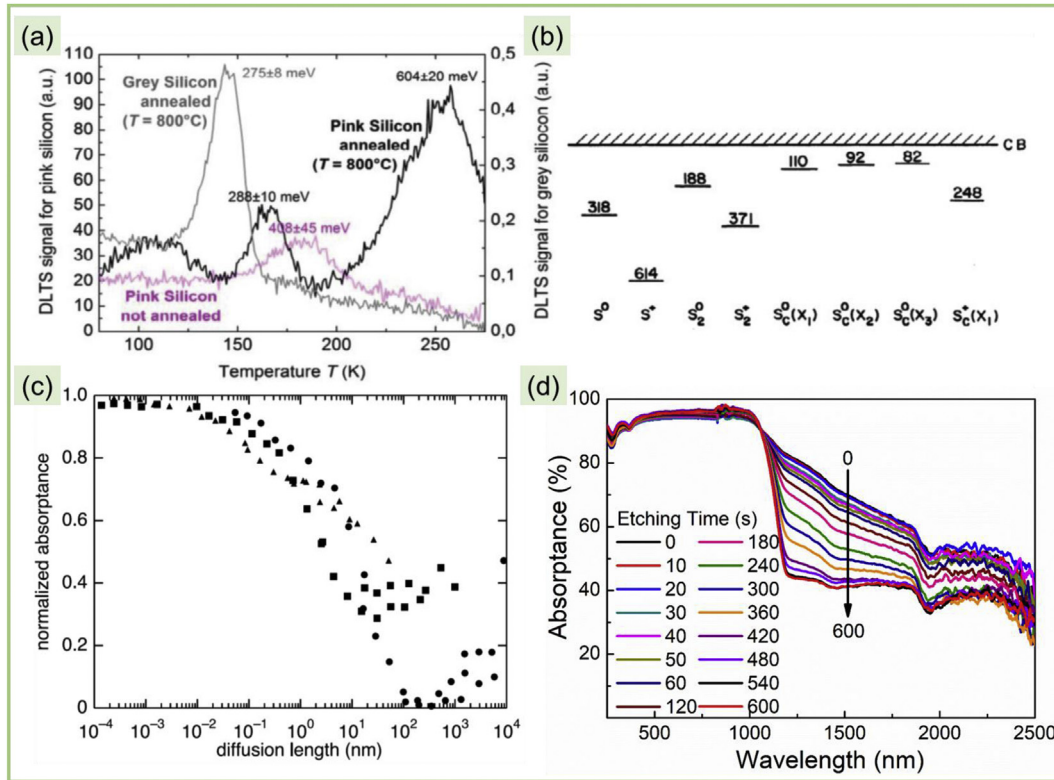


**Fig. 14.** (a) DLTS spectra for annealed, not annealed pink silicon (1 pulse per spot), and annealed grey silicon (5 pulses per spot) [120]. Reproduced with permission. Copyright 2012, Elsevier. (b) S energy levels in the band gap of silicon [149]. Reproduced with permission. Copyright 1984, American Physical Society. (c) Normalized absorbance for S-doped (circles), Se-doped (squares), and Te-doped (triangles) silicon after various thermal anneals versus diffusion length of the respective dopant. The average IR absorbance has been re-normalized, so that the maximum is the pre-annealed value and the minimum is the IR absorbance of the unirradiated silicon wafer [8]. Reproduced with permission. Copyright 2009, Springer-Verlag. (d) Absorption of vacuum black silicon after etching different times [127]. Reproduced with permission. Copyright 2015, IEEE.

techniques [123]. The S-hyperdoped Si with great sub-bandgap absorption contained a higher concentration of  $S^{2-}$  (monosulfide) species. Annealing S-hyperdoped Si reduced the sub-bandgap absorption and the concentration of  $S^{2-}$  species but significantly increased the concentration of larger S clusters [polysulfides ( $S_n^{2-}$ ,  $n > 2$ )] [123,124]. Similarly, the evolution of the chemical state of Se with annealing has been investigated by extended X-ray absorption fine structure spectroscopy, which showed a shift in the chemical state of Se with annealing closely related to the observed decay in the sub-bandgap absorption [125]. Despite the improved understanding of the diffusion-limited kinetics and changes in the chemical state that occur during the annealing of Se-hyperdoped Si, no direct structural evidence of dopant diffusion or phase segregation has been observed [126].

For pulsed-laser-irradiated Si without hyperdoping, the relationship between the sub-bandgap IR absorption and the as-formed new phases (including amorphous Si [ $\alpha$ -Si] and nanocrystalline Si) was established by Li et al. [127]. The relationship indicates that the IR absorption was caused by defects related to the Urbach states from  $\alpha$ -Si or nanocrystalline Si, and these metastable defects disappeared after a thermal annealing process (Fig. 14d). From the absorption spectrum of micro-nanostructured Si after etching at different times, it can be determined that Urbach states existed in both the surface and subsurface regions of black Si at a depth of approximately 2.4  $\mu\text{m}$  [127].

The IR absorption mechanism of black Si has also been theoretically investigated by first-principles calculations [124,128–132]. In addition, the optical response of P-doped Si nanocrystals has been studied by tight-binding calculations [146]. For chalcogen doping, the atomic geometries of defect-related states (high-energy

interstitial, substitutional, and quasi-substitutional sites) appeared in the gap of Si, which played an important role in the optical absorption. Fig. 15a–c shows typical atomic structures [substitutional (a), quasi-substitutional with lowest energy (b), and interstitial with lowest energy (c)], and their formation energies were  $-2.81$  (a),  $-0.23$  (b), and  $-2.63$  eV (c), respectively. Their typical band structures near the Fermi energy are given in Fig. 15d–f. For the substitutional S, the S doping (0.463%) brought about an intermediate band with a width of 0.22 eV in the gap of Si (d). In the lowest energy quasi-substitutional S-doped Si, there were three defect bands near the Fermi energy (e). However, the interstitial configuration of S-doped Si did not introduce any defect states into the gap of Si (f). Molecular dynamics simulations combined with optical absorption calculations have revealed that the annealing-induced reduction in the IR absorption observed in experiments was possibly due to two types of structural transformations: transformations from higher energy interstitial configurations to the lowest energy interstitial configuration and transformations from the quasi-substitutional configurations to the lowest energy interstitial configuration [124,128]. However, the results differed from those of chalcogen doping, and there was more stable sub-bandgap absorption in N-doped Si. The physical mechanism was attributed to the good stability of the substitutional N defect after annealing [130–132].

## 5. Black Si IR PDs

The most promising application based on black Si is NIR PDs [12,13]. Black Si materials can be used to fabricate NIR PDs because of their excellent IR absorption ability. After hyperdoping by an

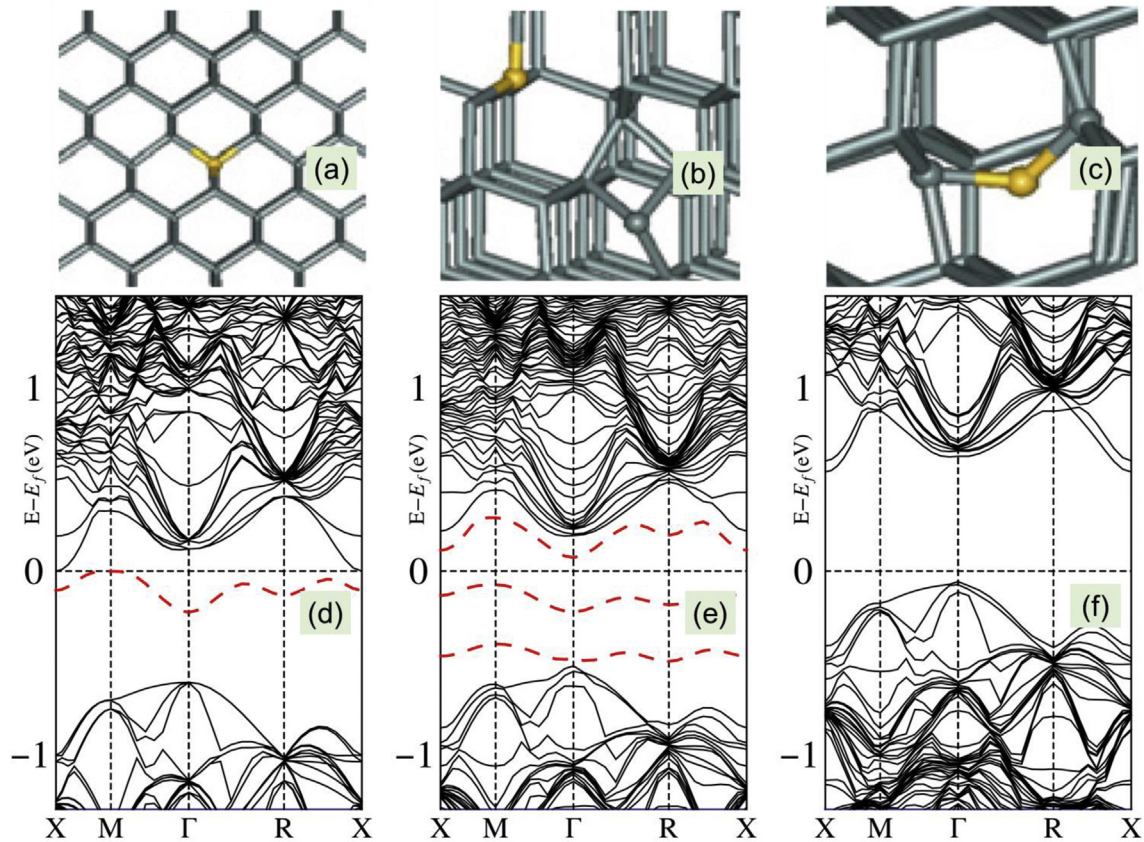


**Fig. 15.** Typical atomic structures with an S atom situated at a substitutional or interstitial position in Si. They were (a)  $S_s$ , (b) lowest energy  $S_{qs}$ , and (c) lowest energy  $S_i$ . Band structures of the substitutional configurations of (d)  $S_s$ , the lowest energy quasi-substitutional ones of (e)  $S_{qs}$ , and the lowest energy interstitial ones of (f)  $S_i$ . The line at zero energy represents the Fermi level. The fractional coordinates of the k-points in the Brillouin zone are  $\Gamma(0, 0, 0)$ ,  $X(0.5, 0, 0)$ ,  $M(0.5, 0.5, 0)$ , and  $R(0.5, 0.5, 0.5)$  [128]. Reproduced with permission. Copyright 2012, EPLA.

ultrafast laser, a device junction can be formed between the hyperdoped Si layer and the Si substrate, for example, a p-n junction [14]. Most studies on detectors based on black Si focused on the current–voltage (I–V) characteristics, responsivity, spectral response, and response time. Carey et al. [15] fabricated a photodiode based on micro-nanostructured Si irradiated by an fs laser (100 fs, 1 kHz) in an  $\text{SF}_6$  atmosphere. A schematic diagram of the photodiode is shown in Fig. 16a. The micro-nanostructured Si photodiode was composed of two heterojunctions: one junction was between the Si substrate c-Si and the micro-nanostructured black Si layer, whereas the other junction was between the substrate and the Cr/Au metal layer. The rectification characteristics of the photodiodes significantly depended on the annealing temperature of the black Si. The responsivity (Fig. 16b) increased with annealing temperature up to 825 K and then decreased. At the optimum annealing temperature of 825 K, the responsivity increased with the bias voltage; however, the leakage current also increased with the bias voltage. In addition, the responsivity decreased with increasing laser fluence. The optimum response was thus obtained at an fs laser fluence of  $4 \text{ kJ/m}^2$  and an annealing temperature of 825 K for micro-nanostructuring. Under these conditions, the peak responsivity reached  $120 \text{ A/W}$  at  $1.0 \mu\text{m}$ , which was two orders of magnitude higher than the responsivity of commercial Si P–I–N photodiodes and similar to that of avalanche photodiodes at the same wavelength. In the NIR region, the responsivity was  $50 \text{ mA/W}$  at  $1.33 \mu\text{m}$  and  $35 \text{ mA/W}$  at  $1.55 \mu\text{m}$ , five orders of magnitude higher than the responsivity of non-micro-nanostructured Si photodiodes [15]. This high photoresponse was

regarded as a direct result of photoconductive gain, which is an amplification mechanism commonly observed in II–VI semiconductors but previously not observed in Si-based material systems [15,16]. Then, Huang et al. [17] fabricated mesa devices using the above micro-nanostructured S-doped Si. The mesas had diameters from 50 to  $500 \mu\text{m}$ . At reverse biases of 1 and 3 V, the dark currents were 1.3 and  $2.3 \mu\text{A}$  for a  $100\text{-}\mu\text{m}$ -diameter device, respectively, more than one order of magnitude lower than the forward-biased dark current at the same voltages. Fig. 16c shows the frequency response of a  $250\text{-}\mu\text{m}$ -diameter device as determined under illumination through a chopper, whose frequency was varied. The bandwidth of the device was approximately 1,200 Hz at a reverse bias of 3 V, and the bandwidth did not vary greatly with the device area [17,18].

The SiOnyx Company reported on CMOS sensors with an enhanced spectral response [11]. Devices were fabricated on eight-inch Si wafers using standard CMOS processes. The detector used an abridged process flow consisting of 10 mask layers. Ultrafast laser fabrication was carried out in an  $\text{SF}_6$  atmosphere. Using this method, S concentrations greater than  $10^{19} \text{ cm}^{-3}$  could be achieved. The measured quantum efficiency (QE) of black-Si-enhanced photovoltaic sensors is shown in Fig. 17, and the black Si fabricated by the ultrafast laser led to dramatically enhanced QE in the  $0.8\text{--}1.2 \mu\text{m}$  range. The data were collected for sufficiently thin detectors (active layer  $< 10 \mu\text{m}$ ) suitable for direct integration into focal plane array architectures. The data showed a direct comparison of the black Si performance with that of a state-of-the-art charge-coupled device (CCD) image sensor and Generation 3

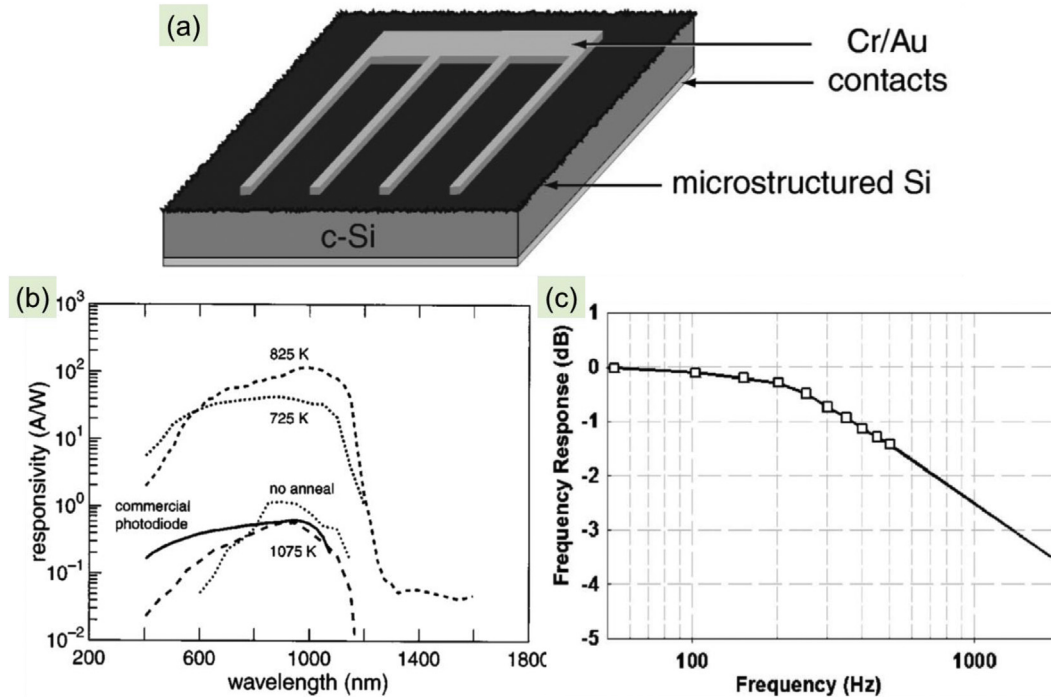


**Fig. 16.** (a) Schematic diagram of a micro-nanostructured silicon photodiode. The disordered surface layer is approximately 300 nm thick, and the substrate wafer is 250  $\mu\text{m}$  thick. (b) Dependence on annealing temperature of the responsivity of micro-nanostructured silicon photodiodes. Each sample was micro-nanostructured with 100 fs laser pulses at a fluence of 4  $\text{kJ}/\text{m}^2$  and annealed 30 min. The responsivity of a commercial silicon P–I–N photodiode is shown for reference. (a) and (b) [15] Reproduced with permission. Copyright 2005, Optical Society of America. (c) Frequency response of a 250- $\mu\text{m}$ -diameter micro-nanostructured Si photodetector at 3 V reverse bias [17]. Reproduced with permission. Copyright 2006, AIP Publishing LLC.

night vision image intensifiers [133,134]. At 0.94  $\mu\text{m}$ , the CCD had a quite small QE of approximately 8%, whereas the black Si device could achieve a QE in excess of 65%. Furthermore, at the critical 1.064  $\mu\text{m}$  wavelength of the YAG laser, where the current Generation 3 night vision device was blind, the QE of the Generation 3 was 30x that of the CCD device. This enhancement was driven by fundamental material changes induced by the ultrafast laser process. Quadrant detectors with black Si were also designed and packaged into ceramic leadless chip carrier (LCC) packages (Fig. 17b). In addition, photolithographic patterning of black Si in an eight-inch CMOS-compatible manufacturing flow was demonstrated (Fig. 17c). This enabled the integration of black Si with traditional manufacturing methods for CMOS image sensing technology. The quadrant detector performance is shown in Table 1 [10,11]. In addition, the reliability data showed no impact on performance after accelerated life testing at 80  $^{\circ}\text{C}$  and 85% relative humidity for a prolonged exposure (250 h).

Se- or Te-hyperdoped black Si obtained by pulsed laser doping also showed a photoresponse to NIR light. The Se- and Te-hyperdoped  $n^+-n$  photodiodes fabricated by fs laser pulses have been reported to exhibit responsivities of 2.41 A/W (bias of  $-12$  V) and 2.4836 A/W (bias of  $-10$  V) at 1.064  $\mu\text{m}$ , respectively [19,135,136]. As another example, Se-doped black Si could be prepared by fs laser irradiation of Si substrates coated with Si/Se bilayer films [137]. The responsivities of the  $n^+-n$  photodiodes at 1.064  $\mu\text{m}$  depended on the thickness of the deposited Se films. At a  $-10$  V bias, the responsivities were 0.310, 0.786, 0.911, and 1.22 A/W for samples prepared with Se film thicknesses of 50, 75, 100, and 125 nm, respectively. In addition, Se-doped black Si was prepared by ps pulsed laser irradiation, and  $n^+-p$  junctions were formed between the Se-doped layers and the p-type Si substrates [20,138]. The photodiodes exhibited an enhanced spectral response from 0.4 to 1.6  $\mu\text{m}$ . At a  $-5$  V bias, room temperature responsivities of 16 A/

W at 1.0  $\mu\text{m}$ , (the much smaller) 15 mA/W at 1.33  $\mu\text{m}$ , and 12 mA/W at 1.55  $\mu\text{m}$  were obtained.

In addition, NIR PDs based on codoped Si have also been reported. For instance, at a  $-12$  V bias, a responsivity of 1.60 A/W at 1.064  $\mu\text{m}$  for an (S, Se)-codoped Si  $n^+-n$  photodiode prepared by fs laser irradiation was obtained [97]. Moreover, at a  $-5$  V bias, a responsivity of 58 mA/W at 1.31  $\mu\text{m}$  was obtained based on an (S, N)-codoped black Si photodiode fabricated by fs laser irradiation [98]. For the above black Si materials supersaturated with different dopants, defect-related states were introduced into the gap of Si by hyperdoping. Then, these electronic states as the origin of the NIR absorption (e.g. at 1.31 and 1.55  $\mu\text{m}$ ) of hyperdoped Si could contribute to the presented NIR photoresponse.

To our surprise, undoped black Si photodiodes also showed a remarkable sub-bandgap photoresponse. The undoped black Si was fabricated on the surface of a near-intrinsic Si substrate by ns laser direct writing in an Ar atmosphere [21,139]. The resistivity of the ns-laser-irradiated black Si layer was approximately five orders of magnitude lower than that of the unprocessed Si substrate. NIR Si  $n^+-n$  photodiodes were produced based on the difference in the carrier concentration between the black Si layer and the Si substrate. The responsivity of the black Si photodiode for 1.31  $\mu\text{m}$  was up to 256 mA/W at a  $-5$  V bias (Fig. 18a), which was the highest level for 1.31  $\mu\text{m}$  among the laser-irradiated black Si detectors and was much higher than that of the reported pure Si bulk-structure photodiodes. At the same time, the black Si PD at a low reverse bias showed a large gain for VIS–NIR light above the bandgap (8 A/W at  $-5$  V and 0.96  $\mu\text{m}$ ; Fig. 18b). The gain mechanism could be attributed to the photoconductive gain, which was most likely to be the generation–recombination that originated from random carrier generation and recombination in the high-density structural defects in the black Si layer [17]. Therefore, structural defects, which can introduce energy levels into the gap of Si, seem to be the key

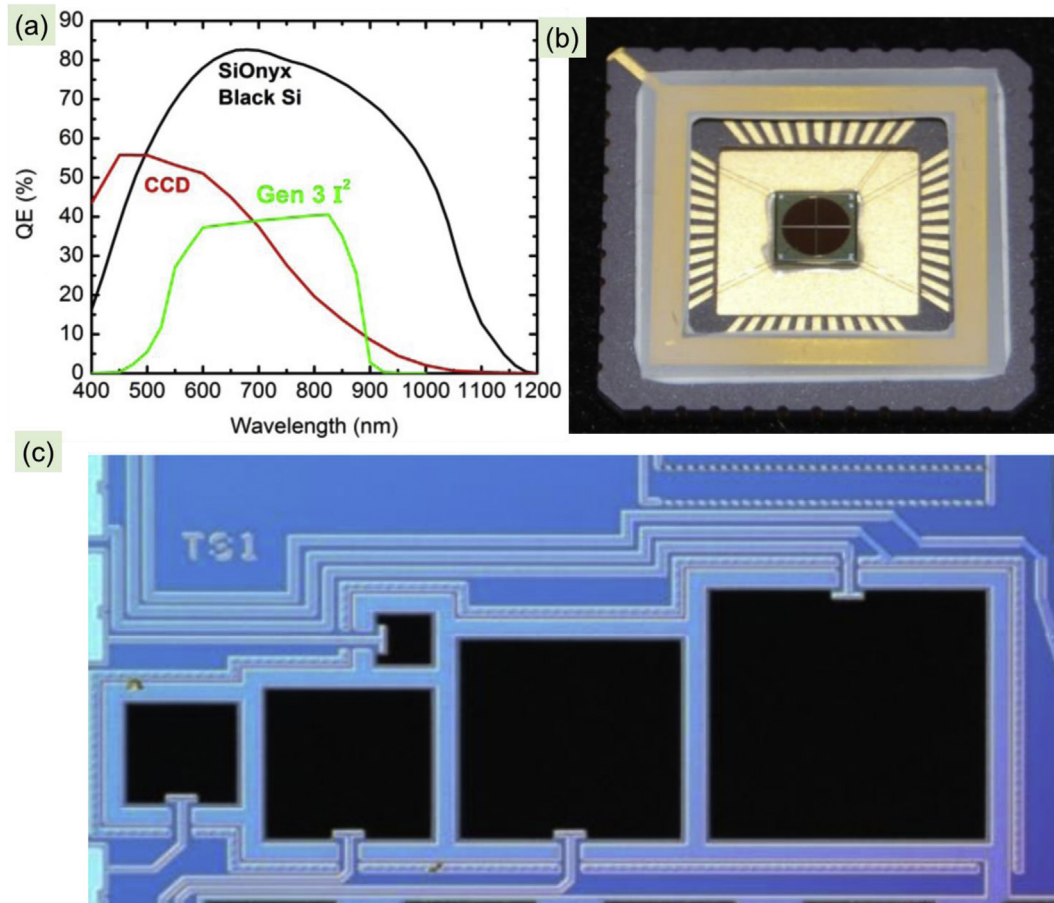


**Fig. 17.** (a) External quantum efficiency for a thin ( $<10\ \mu\text{m}$ ) black silicon photodiode (black) measured in photovoltaic mode as compared to industry leading CCD imaging sensor (red) and Generation 3 image intensifier night vision (green) [133,134]. (b) Quad detector packaged in LCC package. (c) Eight-inch CMOS-fabricated photodiodes of black silicon [11]. Reproduced with permission. Copyright 2011, SPIE.

**Table 1**

The black-silicon Quad detector performance [11].

Parameter	SiOnyx
Device type	Quad (bulk)
Response (1.064 $\mu\text{m}$ )	0.58 A/W
Bias voltage	20 V
Capacitance	8 pF
Dark current ( $-5\ \text{V}$ )	400 pA/cm <sup>2</sup>
Response time	10 ns

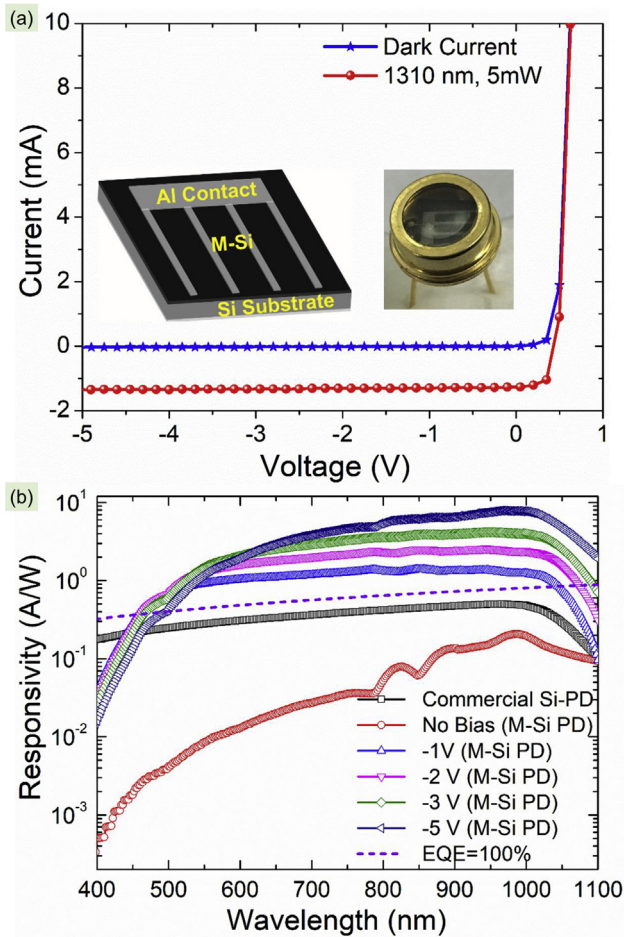
factor contributing to the photoresponse. The fact that the device based on micro-nanostructured Si does not respond as fast as that based on c-Si is also due to structural defects [147].

Table 2 lists the typical Si PDs based on black Si materials obtained using different laser pulses and dopants. Fig. 19 shows the history of the progress in black Si PDs corresponding to Table 2. Fig. 19a and b shows the responsivity below (abnormal detection) and above (normal detection) the bandgap of Si, respectively. The main affiliations are listed in this figure. A PD based on S-doped black Si was first reported in 2005 [15]. After that, some other black Si PDs were also reported, such as Se-doped, Te-doped, N-doped, co-doped (S, N or S, Se), and non-doped black Si devices. From Table 2, the S-doped black Si (after fs laser irradiation) PD made by Harvard University showed the largest responsivity (95 A/W at  $-0.5\ \text{V}$ ) to  $1.06\ \mu\text{m}$  ( $\lambda < 1.1\ \mu\text{m}$ ) [15]. Gain of the photoresponse to the energy above the bandgap of Si also appeared for Se-doped and

Te-doped black Si PDs [19,20,135–138]. However, the non-doped black Si (after ns laser irradiation) PD made by Jilin University had the most distinct photoresponse (0.26 A/W at  $-5\ \text{V}$ ) to  $1.31\ \mu\text{m}$  ( $\lambda > 1.1\ \mu\text{m}$ ) [21]. In addition, a photoresponse to  $1.31\ \mu\text{m}$  was observed in the S-doped black Si (fs pulsed laser) [15,17], Se-doped black Si (ps pulsed laser) [20], N-doped black Si (fs pulsed laser) [87], and S–N-codoped black Si (fs pulsed laser) [96] devices.

## 6. Summary and prospects

This review provides the main properties and PD applications of black Si materials fabricated by ultrafast laser pulses. After irradiation with ultrafast laser pulses, the Si surface melts and ablates when the laser fluence exceeds the ablation threshold of c-Si. As a result, LIPSS form. We discussed the dependence of the black Si surface morphology on the background atmosphere, substrate temperature, and laser parameters. If a dopant is present in the fabrication system, then impurities can be doped into the melted surface layer and be trapped in this layer because of the subsequent resolidification process. Therefore, a supersaturated impurity with a low solid solubility in c-Si can be hyperdoped into black Si by the ultrafast laser pulse process. In this review, we discussed the common dopants used in preparing black Si, such as chalcogen (S, Se, Te), N, P, and Au elements, and their codoping. With hyperdoping, an impurity band may be introduced into the bandgap of Si and contribute to the IR absorption. With surface texturing, this IR absorption will be further enhanced. Apart from the contribution



**Fig. 18.** (a) Photo current and dark current versus voltage characteristics for the IR photodetector of the black Si. (b) Responsivity of the M-Si PD for several reverse biases. Responsivity of a commercial Si-PD is shown for reference. The EQE of 100% versus wavelength is shown as a short-dashed line [21]. Reproduced with permission. Copyright 2018, IEEE.

from the impurity band, the IR absorption of black Si may also arise from laser-induced structural defects and free carrier absorption. However, the excellent IR absorption characteristics of black Si are not thermostable for many black Si materials. The reason for the

poor thermal stability of the IR absorption may be related to the diffusion of the dopants, transformation of the chemical states or (electronic and atomic) structures in hyperdoped Si, and unstable structural defects such as the Urbach state, which have been discussed in the review. Based on the good IR absorption nature, black Si materials have been applied in the field of IR photodetection. Currently, a responsivity of 120 A/W at 1.0 μm (within the absorption edge) has been obtained for an S-doped Si PD. Furthermore, a responsivity of 0.26 A/W at 1.31 μm (below the bandgap) was observed for an undoped black Si IR PD.

In the future, to obtain IR Si PDs with high performance, the following challenges should be addressed:

- A large surface roughness implies folding of a flat surface to increase the surface area to obtain more photons in textured Si PDs. Although surface texturing is beneficial to IR absorption enhancement, it is not a good choice for manufacturing Si PDs because obtaining a large surface roughness with lithography patterning is challenging. In addition, a large surface roughness can increase the surface recombination of photogenerated carriers and, as a result, reduce the lifetime of non-equilibrium carriers. Therefore, choosing the proper laser fluence for the fabrication of black Si may be more advantageous for the application of a photoelectric conversion device.
- Selecting an appropriate dopant is very important for obtaining black Si with NIR absorption. A deep-level impurity is necessary, such as chalcogen and transition metal elements, because these impurities can introduce energy levels into the gap of Si. In contrast, a shallow-level impurity, such as a III–V group impurity (except for N), is not suitable. At the same time, shallow-level impurities can produce a higher background free carrier concentration in black Si, resulting in large free carrier absorption, which is undesirable for device applications because of the lowering of the IR responsivity. In addition, considering the thermostability of the IR absorption of black Si materials, an impurity with a high diffusion rate in c-Si is not suitable for black Si fabrication (such as the alkali metal impurities Li, Na, and K). Therefore, it is necessary to select a proper impurity for pulsed laser doping of black Si.
- Considering the uniformity of the rectifying junction formed between the doped black Si layer and the Si substrate, a solid dopant (film or powder) is not as good as a gaseous dopant. However, solid dopants can provide more choices for the doping element. Therefore, in the future, improving the continuity and uniformity of the doped black Si layer will be a focusing issue.

**Table 2**

The dopant, laser pulses width, contact junction, responsivity, response wavelength, and corresponding reverse bias of black silicon photodetectors.

Dopant	Pulses width	Contact junction	Responsivity (A/W)	Response wavelength (μm)	Reverse bias (V)	Reference
Sulfur	100 fs	n <sup>+</sup> –n	95	1.06	–0.5	[15]
			0.05	1.31		
			0.035	1.55		
Sulfur	100 fs	n <sup>+</sup> –n, Schottky	55	1.06	–3	[17]
			0.09	1.33		
			0.02	1.55		
			0.69	0.8		
Sulfur	100 fs	n <sup>+</sup> –p	0.58	1.064	–5	[16]
Sulfur	100 fs	CMOS	0.58	1.064	–20	[11]
Selenium	100 fs	n <sup>+</sup> –n	2.41	1.064	–12	[19]
Selenium	100 fs	n <sup>+</sup> –n	1.22	1.064	–10	[137]
Selenium	30 ps	n <sup>+</sup> –p	16	1.0	–5	[20]
			0.015	1.33		
			0.012	1.55		
Selenium	30 ps	n <sup>+</sup> –p	30	1.06	–3	[138]
Tellurium	100 fs	n <sup>+</sup> –n	2.4836	1.064	–10	[135, 136]
Nitrogen	100 fs	Schottky	0.0053	1.31	–10	[87]
Sulfur and Nitrogen	100 fs	n <sup>+</sup> –n, Schottky	0.058	1.31	–10	[96]
No doping	10 ns	n <sup>+</sup> –n	0.26	1.31	–5	[21]

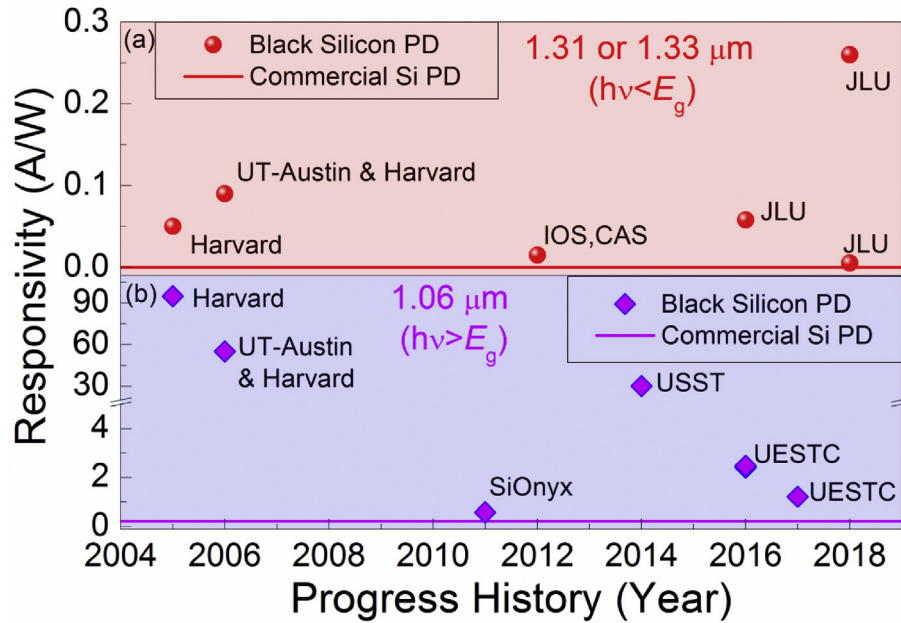


**Fig. 19.** Progress history of the black silicon photodetectors. The responsivity corresponds to the data and the references in Table 2. (a) The responsivity of black silicon photodetectors for the infrared light of energy below the bandgap of silicon (abnormal detection); and (b) the responsivity of black silicon photodetectors for the infrared light of energy above the bandgap of silicon (normal detection). The main affiliation is listed in this figure.

• Thermal annealing causes deactivation of the sub-bandgap optical absorption. Different from thermal annealing, laser annealing has little effect on the sub-bandgap absorption of black Si. Therefore, to maintain the NIR absorption, another research interest should be focusing on the annealing process, such as rapid thermal annealing or laser annealing.

In summary, pulsed-laser-induced black Si shows strong IR absorption and IR detection ability. Based on the perfect compatibility of Si with the current mature CMOS technology, black Si will make an important contribution in the integrated optoelectronics field if the above difficulties can be finally overcome.

#### Conflict of interest statement

The authors declare that they have no known competing financial interests or personal relationships that could have appeared to influence the work reported in this paper.

#### Acknowledgements

This work was supported by National Natural Science Foundation of China (NSFC) under grants #61775077, #61922035, #61590930, #11874171 and #61960206003. Prof. Ji-Hong Zhao acknowledges Center of Ultrafast Optoelectronic Technologies (C-UFO) for more than 10 year supports on the black-silicon research.

#### References

- [1] Intel Corporation. Moor's law, made real by Intel innovations. <http://www.intel.com/technology/mooreslaw/index.htm>.
- [2] S.E. Miller, QE-8, IEEE J. Quantum Electron (1972) 199.
- [3] S.O. Kasap, Optoelectronics and Photonics Principles and Practices, New Jersey, Prentice-Hall International, USA, 2001.
- [4] M. Paniccia, Silicon Photonics Applications Research Results and Integration Challenges, Berkeley Lecture Series, USA, 2004.
- [5] T.-H. Her, R.J. Finlay, C. Wu, S. Deliwala, E. Mazur, Appl. Phys. Lett. 73 (1998) 1673.
- [6] C. Wu, C.H. Crouch, L. Zhao, J.E. Carey, R. Younkin, J.A. Levinson, E. Mazur, R.M. Farrell, P. Gothoskar, A. Karger, Appl. Phys. Lett. 78 (2001) 1850.
- [7] R. Younkin, J.E. Carey, E. Mazur, J.A. Levinson, C.M. Friend, J. Appl. Phys. 93 (2003) 2626.
- [8] B.R. Tull, M.T. Winkler, E. Mazur, Appl. Phys. A 96 (2009) 327.
- [9] <https://www.sionyx.com/>.
- [10] J.E. Carey, J. Sickler, IR Detectors: Black Si Sees Further into the IR, Laser Focus World, 2009. <https://www.laserfocusworld.com/articles/print/volume-45/issue-8/features/ir-detectors-black-silicon-sees-further-into-the-ir.html>.
- [11] M.U. Pralle, J.E. Carey, H. Homayoon, J. Sickler, X. Li, J. Jiang, D. Miller, C. Palsule, J. McKee, Proc. SPIE 2011 8012 (2011) 801222.
- [12] R.A. Myers, R. Farrell, A.M. Karger, J.E. Carey, E. Mazur, Appl. Optic. 45 (2006) 8825.
- [13] K. Yamamoto, A. Sakamoto, T. Nagano, K. Fukumitsu, Nucl. Instrum. Methods Phys. Res. A 624 (2010) 520.
- [14] P. Saring, A.L. Baumann, B. Schlieper-Ludewig, S. Kontermann, W. Schade, M. Seibt, Appl. Phys. Lett. 103 (2013), 061904.
- [15] J.E. Carey, C.H. Crouch, M. Shen, E. Mazur, Opt. Lett. 30 (2005) 1773.
- [16] J.-H. Zhao, C.-H. Li, Q.-D. Chen, H.-B. Sun, IEEE Sensor. J. 15 (2015) 4259.
- [17] Z. Huang, J.E. Carey, M. Liu, X. Guo, E. Mazur, J.C. Campbell, Appl. Phys. Lett. 89 (2006), 033506.
- [18] Z. Li, B.K. Nayak, V.V. Iyengar, D. McIntosh, Q. Zhou, M.C. Gupta, C. Campbell, Appl. Optic. 50 (2011) 2508.
- [19] L. Du, Z. Wu, R. Li, F. Tang, Y. Jiang, Opt. Lett. 41 (2016) 5031.
- [20] S. Hu, P. Han, S. Wang, X. Mao, X. Li, L. Gao, Semicond. Sci. Technol. 27 (2012) 102002.
- [21] J.-H. Zhao, C.-H. Li, X.-B. Li, Q.-D. Chen, Z.-G. Chen, H.-B. Sun, IEEE Trans. Electron. Dev. 65 (2018) 4905.
- [22] T. Gimpel, K.-M. Guenther, S. Kontermann, W. Schade, Appl. Phys. Lett. 105 (2014), 053504.
- [23] X. Zhu, H. Zhu, D. Liu, Y. Huang, X. Wang, H. Yu, S. Wang, X. Lin, P. Han, Adv. Mater. Res. 418–420 (2011) 217.
- [24] B.K. Nayak, V.V. Iyengar, M.C. Gupta, Prog. Photovoltaics Res. Appl. 19 (2011) 631.
- [25] B.K. Nayak, V. Iyengar, M.C. Gupta, Mater. Res. Soc. Symp. Proc. 1123 (2009) 7.
- [26] Z.-X. Yan, C.-H. Li, Y. Luo, J.-H. Zhao, H. Yang, P. Verma, S. Kawata, Chin. Optic Lett. 13 (2015) 102401.
- [27] C. Wu, C.H. Crouch, L. Zhao, E. Mazur, Appl. Phys. Lett. 81 (2002) 1999.
- [28] Q. Lü, J. Wang, C. Liang, L. Zhao, Z. Jiang, Opt. Lett. 38 (2013) 1274.
- [29] T. Chen, J. Si, X. Hou, S. Kanehira, K. Miura, K. Hirao, J. Appl. Phys. 110 (2011), 073106.
- [30] T. Baldacchini, J.E. Carey, M. Zhou, E. Mazur, Langmuir 22 (2006) 4917.
- [31] H.O. Jeschke, M.E. Garcia, M. Lenzner, J. Bonse, J. Krüger, W. Kautek, Appl. Surf. Sci. 197–198 (2002) 839.
- [32] M.-J. Sher, M.T. Winkler, E. Mazur, MRS Bull. 36 (2011) 439.
- [33] A.Y. Vorobyev, C. Guo, Appl. Surf. Sci. 257 (2011) 7291.
- [34] Q. Wang, W. Zhou, Opt. Mater. 72 (2017) 508.
- [35] M. Shen, J.E. Carey, C.H. Crouch, M. Kandyla, H.A. Stone, E. Mazur, Nano Lett. 8 (2008) 2870.

- [36] G. Miyaji, K. Zhang, J. Fujita, K. Miyazaki, *J. Laser Micro/Nano Eng.* 7 (2012) 198.
- [37] M. Sobhani, M.H. Mahdieh, *Laser Part. Beams* 31 (2013) 465.
- [38] E.V. Barmina, C. Fotakis, P.A. Loukakos, E. Stratakis, G.A. Shafeev, *Appl. Phys. A* 117 (2014) 359.
- [39] M. Sobhani, M.H. Mahdieh, *Laser Phys.* 25 (2015), 056101.
- [40] J. Meng, H. Song, X. Li, S. Liu, *Appl. Phys. A* 118 (2015) 1197.
- [41] M.A. Sheehy, L. Winston, J.E. Carey, C.M. Friend, E. Mazur, *Chem. Mater.* 17 (2005) 3582.
- [42] H. Yang, X. Li, G. Li, C. Wen, R. Qiu, W. Huang, J. Wang, *Appl. Phys. A* 104 (2011) 749.
- [43] C. Wen, H.D. Yang, X.H. Li, Y.X. Cui, X.Q. He, X.F. Duan, Z.H. Li, *Appl. Phys. A* 109 (2012) 635.
- [44] J. J.J. Nivas, Z. Song, R. Fittipaldi, A. Vecchione, R. Bruzzese, S. Amoruso, *Appl. Surf. Sci.* 417 (2017) 149.
- [45] J. J.J. Nivas, F. Gesuele, E. Allahyari, S.I. Oscurato, R. Fittipaldi, A. Vecchione, R. Bruzzese, S. Amoruso, *Opt. Lett.* 42 (2017) 2710.
- [46] J. J.J. Nivas, E. Allahyari, F. Gesuele, P. Maddalena, R. Fittipaldi, A. Vecchione, R. Bruzzese, S. Amoruso, *Appl. Phys. A* 124 (2018) 198.
- [47] J. Thorstensen, S.E. Foss, *J. Appl. Phys.* 112 (2012) 103514.
- [48] G. Deng, G. Feng, S. Zhou, *Optic Express* 25 (2017) 7818.
- [49] K. Luo, X. Chen, Y. Peng, Y. Zhu, *Appl. Optic.* 55 (2016) 6079.
- [50] J. J.J. Nivas, S. He, Z. Song, A. Rubano, A. Vecchione, D. Paparo, L. Marrucci, R. Bruzzese, S. Amoruso, *Appl. Surf. Sci.* 418 (2017) 565.
- [51] Y. Peng, Y. Zhou, X. Chen, Y. Zhu, *Optic Commun.* 334 (2015) 122.
- [52] Y. Peng, Y. Wen, D. Zhang, S. Luo, L. Chen, Y. Zhu, *Appl. Optic.* 50 (2011) 4765.
- [53] G. Nava, R. Osellame, R. Ramponi, K.C. Vishnubhatla, *Opt. Mater. Express* 3 (2013) 612.
- [54] B.R. Tull, J.E. Carey, E. Mazur, J.P. McDonald, S.M. Yalisove, *MRS Bull.* 31 (2006) 626.
- [55] Y. Peng, M. Hong, Y. Zhou, D. Fang, X. Chen, B. Cai, Y. Zhu, *Appl. Phys. Express* 6 (2013), 051303.
- [56] Y. Peng, D. Zhang, H. Chen, Y. Wen, S. Luo, L. Chen, K. Chen, Y. Zhu, *Appl. Optic.* 51 (2012) 635.
- [57] Y. Peng, H. Chen, C. Zhu, D. Zhang, Y. Zhou, H. Xiang, B. Cai, Y. Zhu, *Mater. Lett.* 83 (2012) 127.
- [58] Y. Ma, J. Si, X. Sun, T. Chen, X. Hou, *Appl. Surf. Sci.* 313 (2014) 905.
- [59] J. Zhu, Y. Shen, W. Li, X. Chen, G. Yin, D. Chen, L. Zhao, *Appl. Surf. Sci.* 252 (2006) 2752.
- [60] J. Zhu, W. Li, M. Zhao, G. Yin, X. Chen, D. Chen, L. Zhao, *Proc. SPIE* 5629 (2005) 276. Bellingham, WA (2005).
- [61] B.K. Nayak, M.C. Gupta, *Appl. Optic.* 51 (2012) 114.
- [62] M.A. Bassam, P. Parvin, B. Sajad, A. Moghimi, H. Coster, *Appl. Surf. Sci.* 254 (2008) 2621.
- [63] H.R. Dehghanpour, P. Parvin, B. Sajad, S.S. Nour-Azar, *Appl. Surf. Sci.* 255 (2009) 4664.
- [64] W.-T. Hsiao, S.-F. Tseng, K.-C. Huang, Y.-H. Wang, M.-F. Chen, *Int. J. Adv. Manuf. Technol.* 56 (2011) 223.
- [65] S. Binetti, A. Le Donne, A. Rolfi, B. Jäggi, B. Neuenschwander, C. Busto, C. Frigeri, D. Scorticati, L. Longoni, S. Pellegrino, *Appl. Surf. Sci.* 371 (2016) 196.
- [66] S. Sarbada, Z. Huang, Y.C. Shin, X. Ruan, *Appl. Phys. A* 122 (2016) 453.
- [67] A.J. Pedraza, J.D. Fowlkes, D.H. Lowndes, *Appl. Phys. Lett.* 74 (1999) 2322.
- [68] M. Sardar, J. Chen, Z. Ullah, M. Jelani, A. Tabassum, J. Cheng, Y. Sun, J. Lu, *Mater. Res. Express* 4 (2017) 125902.
- [69] X. Li, L. Chang, R. Qiu, C. Wen, Z. Li, S. Hu, *Appl. Surf. Sci.* 258 (2012) 8002.
- [70] C.H. Crouch, J.E. Carey, J.M. Warrenner, M.J. Aziz, E. Mazur, F.Y. Génin, *Appl. Phys. Lett.* 84 (2004) 1850.
- [71] V. Zorba, N. Boukos, I. Zergioti, C. Fotakis, *Appl. Optic.* 47 (2008) 1846.
- [72] X. Zhan, H. Xu, C. Li, H. Zang, C. Liu, J. Zhao, H. Sun, *Opt. Lett.* 42 (2017) 510.
- [73] M. Sher, N.M. Mangan, M.J. Smith, Y. Lin, S. Marbach, T.M. Schneider, S. Gradečak, M.P. Brenner, E. Mazur, *J. Appl. Phys.* 117 (2015) 125301.
- [74] J. Bonsea, K.-W. Brzezinka, A.J. Meixner, *Appl. Surf. Sci.* 221 (2004) 215.
- [75] T. Gimpel, Ingmar Höger, F. Falk, W. Schade, S. Kontermann, *Appl. Phys. Lett.* 101 (2012) 111911.
- [76] P. Saring, A.L. Baumann, S. Kontermann, W. Schade, M. Seibt, *Solid State Phenom.* 205–206 (2013) 358.
- [77] M.J. Smith, Y. Lin, M. Sher, M.T. Winkler, E. Mazur, S. Gradečak, *J. Appl. Phys.* 110 (2011), 053524.
- [78] M.J. Smith, M. Sher, B. Franta, Y. Lin, E. Mazur, S. Gradečak, *J. Appl. Phys.* 112 (2012), 083518.
- [79] A. Kailer, Y.G. Gogotsi, K.G. Nickel, *J. Appl. Phys.* 81 (1997) 3057.
- [80] H. Mei, C. Wang, J. Yao, Y.-C. Chang, J. Cheng, Y. Zhu, S. Yin, C. Luo, *Optic Commun.* 284 (2011) 1072.
- [81] Y. Lin, N. Mangan, S. Marbach, T.M. Schneider, G. Deng, S. Zhou, M.P. Brenner, E. Mazur, *Appl. Phys. Lett.* 106 (2015), 062105.
- [82] M.T. Winkler, M. Sher, Y. Lin, M.J. Smith, H. Zhang, S. Gradečak, E. Mazur, *J. Appl. Phys.* 111 (2012), 093511.
- [83] K.-M. Guenther, T. Gimpel, S. Kontermann, W. Schade, *Appl. Phys. Lett.* 102 (2013) 202104.
- [84] M.-J. Sher, E. Mazur, *Appl. Phys. Lett.* 105 (2014), 032103.
- [85] J. SICKEL, A. Ahrens, A.L. Baumann, W. Schade, S. Kontermann, M. Seibt, *Phys. Status Solidi A* 214 (2017) 1700264.
- [86] X. Dong, N. Li, Z. Zhu, H. Shao, X. Rong, C. Liang, H. Sun, G. Feng, L. Zhao, J. Zhuang, *Appl. Phys. Lett.* 104 (2014), 091907.
- [87] C.-H. Li, X.-P. Wang, J.-H. Zhao, D.-Z. Zhang, X.-Y. Yu, X.-B. Li, J. Feng, Q.-D. Chen, S.-P. Ruan, H.-B. Sun, *IEEE Sensor. J.* 18 (2018) 3595.
- [88] M.J. Smith, M. Winkler, M.-J. Sher, Y.-T. Lin, E. Mazur, S. Gradečak, *Appl. Phys. A* 105 (2011) 795.
- [89] L. Du, Z. Wu, Y. Su, R. Li, F. Tang, S. Li, T. Zhang, Y. Jiang, *Mater. Sci. Semicond. Process.* 54 (2016) 51.
- [90] M.J. Smith, M.-J. Sher, B. Franta, Y.-T. Lin, E. Mazur, S. Gradečak, *Appl. Phys. A* 114 (2014) 1009.
- [91] G. Haberer, M.J. Smith, J.-C. Idrobo, G. Auvert, M.-J. Sher, M.T. Winkler, E. Mazur, N. Gambacorti, S. Gradečak, P. Bleuët, *Microsc. Microanal.* 19 (2013) 716.
- [92] C.-H. Li, J.-H. Zhao, X.-Y. Yu, Q.-D. Chen, J. Feng, H.-B. Sun, *IEEE Photon. J.* 8 (2016) 6805809.
- [93] M. Quigley, D. Liu, H.K. Park, D.X. Yu, D.J. Hwang, *Proc. SPIE* 8607 (2013) 860717.
- [94] X.-Y. Yu, J.-H. Zhao, C.-H. Li, Q.-D. Chen, H.-B. Sun, *IEEE Trans. Nanotechnol.* 16 (2017) 502.
- [95] H. Sun, C. Liang, G. Feng, Z. Zhu, J. Zhuang, L. Zhao, *Opt. Mater. Express* 6 (2016) 1321.
- [96] X.-Y. Yu, Z.-H. Lv, C.-H. Li, X. Han, J.-H. Zhao, *IEEE Sensor. J.* 16 (2016) 5227.
- [97] S. Li, Z. Wu, L. Du, Y. Shi, F. Tang, R. Li, Y. Jiang, *J. Mater. Sci. Mater. Electron.* 29 (2018) 288.
- [98] J.-H. Zhao, Z.-H. Lv, C.-H. Li, X.-Y. Yu, X.-B. Li, *IEEE Sensor. J.* 17 (2017) 1000.
- [99] A.Y. Vorobyev, C. Guo, *Optic Express* 19 (2011) A1031.
- [100] Y. Li, G. Feng, L. Zhao, *Adv. Mater. Res.* 287–290 (2011) 364.
- [101] C.H. Crouch, J.E. Carey, M. Shen, E. Mazur, F.Y. Génin, *Appl. Phys. A* 79 (2004) 1635.
- [102] D. Liu, Y. Huang, X. Zhu, X. Wang, H. Yu, X. Lin, M. Chen, H. Zhu, *Adv. Mater. Res.* 418–420 (2011) 77.
- [103] Y. Wang, S. Liu, Y. Wang, G. Feng, J. Zhu, L. Zhao, *Mater. Lett.* 63 (2009) 2718.
- [104] Y. Wang, J. Gao, H. Yang, X. Wang, *J. Mater. Sci. Mater. Electron.* 27 (2016) 9002.
- [105] Y. Ma, H. Ren, J. Si, X. Sun, H. Shi, T. Chen, F. Chen, X. Hou, *Appl. Surf. Sci.* 261 (2012) 722.
- [106] L. Du, Z. Wu, F. Tang, R. Li, Y. Jiang, *Proc. SPIE* 9686 (2016) 96860Y.
- [107] M.-J. Sher, Y.-T. Lin, M.T. Winkler, E. Mazur, C. Pruner, A. Asenbaum, *J. Appl. Phys.* 113 (2013), 063520.
- [108] Q. Zhu, M. Shen, *Inter. J. Smart Nano Mater.* 6 (2015) 113.
- [109] J. Zhu, L. Zhao, W. Li, Y. Wang, G. Feng, Z. Wang, *Mater. Lett.* 60 (2006) 2187.
- [110] Y. Liu, S. Liu, Y. Wang, G. Feng, J. Zhu, L. Zhao, *Laser Phys.* 18 (2008) 1148.
- [111] X. Dong, N. Li, C. Liang, H. Sun, G. Feng, Z. Zhu, H. Shao, X. Rong, L. Zhao, J. Zhuang, *Appl. Phys. Express* 6 (2013), 081301.
- [112] H. Sun, J. Xiao, S. Zhu, Y. Hu, G. Feng, J. Zhuang, L. Zhao, *Mater* 10 (2017) 351.
- [113] Y. Xuan, T. Zhang, B. Liu, R. Yang, W. Ahmad, Z. Liu, Z. Chen, S. Li, *Phys. Status Solidi A* 213 (2016) 2855.
- [114] Y. Peng, X. Chen, Y. Zhou, G. Xu, B. Cai, Y. Zhu, J. Xu, R. Henderson, J. Dai, *J. Appl. Phys.* 116 (2014), 073102.
- [115] Y. Peng, X.Q. Chen, Y.Y. Zhou, K. Luo, J. Xu, R. Henderson, J.M. Dai, Y.M. Zhu, *Europhys. Lett.* 110 (2015) 68005.
- [116] L.-P. Cao, Z.-D. Chen, C.-L. Zhang, J.-H. Yao, *Front. Phys.* 10 (2015) 107801.
- [117] C. Wen, W. Chen, Y.P. Chen, K.J. Liu, X.H. Li, S.F. Hu, Y.J. Yang, *Mater. Res. Bull.* 93 (2017) 238.
- [118] B. Franta, D. Pastor, H.H. Gandhi, P.H. Rekemeyer, S. Gradečak, M.J. Aziz, E. Mazur, *J. Appl. Phys.* 118 (2015) 225303.
- [119] B.K. Newman, M.-J. Sher, E. Mazur, T. Buonassisi, *Appl. Phys. Lett.* 98 (2011) 251905.
- [120] A.L. Baumann, K.-M. Guenther, P. Saring, T. Gimpel, S. Kontermann, M. Seibt, W. Schade, *Energy Procedia* 27 (2012) 480.
- [121] M.A. Sheehy, B.R. Tull, C.M. Friend, E. Mazur, *Mater. Sci. Eng. B* 137 (2007) 289.
- [122] A.A. Ionin, S.I. Kudryashov, S.V. Makarov, N.N. Mel'nik, A.A. Rudenko, P.N. Saltuganov, L.V. Seleznev, D.V. Sinityn, I.A. Timkin, R.A. Khmel'nikiy, *JETP Lett* 100 (2014) 55.
- [123] M.V. Limaye, S.C. Chen, C.Y. Lee, L.Y. Chen, S.B. Singh, Y.C. Shao, Y.F. Wang, S.H. Hsieh, H.C. Hsueh, J.W. Chiou, C.H. Chen, L.Y. Jang, C.L. Cheng, W.F. Pong, Y.F. Hu, *Sci. Rep.* 5 (2015) 11466.
- [124] K.-F. Wang, H. Shao, K. Liu, S. Qu, Y. Wang, Z. Wang, *Appl. Phys. Lett.* 107 (2015) 112106.
- [125] B. Newman, J. Sullivan, M. Winkler, M. Sher, M. Marcus, S. Fakra, M. Smith, S. Gradečak, E. Mazur, T. Buonassisi, 24th EU PVSEC 236, 2009.
- [126] B.K. Newman, E. Ertekin, J.T. Sullivan, M.T. Winkler, M.A. Marcus, S.C. Fakra, M.-J. Sher, E. Mazur, J.C. Grossman, T. Buonassisi, *J. Appl. Phys.* 114 (2013) 133507.
- [127] C.-H. Li, J.-H. Zhao, Q.-D. Chen, J. Feng, W.-T. Zheng, H.-B. Sun, *IEEE Photon. Technol. Lett.* 27 (2015) 1481.
- [128] H. Shao, Y. Li, J. Zhang, B.-Y. Ning, W. Zhang, X.-J. Ning, L. Zhao, J. Zhuang, *Europhys. Lett.* 99 (2012) 46005.
- [129] H. Jiang, C. Chen, *J. Phys. Chem. A* 119 (2015) 3753.
- [130] Z. Zhu, H. Shao, X. Dong, N. Li, B.-Y. Ning, X.-J. Ning, L. Zhao, J. Zhuang, *Sci. Rep.* 5 (2015) 10513.
- [131] X. Dong, Y. Wang, X. Song, *Appl. Phys. Express* 11 (2018), 011303.
- [132] X. Dong, Y. Wang, X. Song, F. Yang, *Appl. Phys. Express* 11 (2018), 031303.
- [133] E. Bender, in: Lucien M. Biberman (Ed.), *Electro-Optical Imaging: System Performance and Modeling*, SPIE press, 2000 (Chapter 5).
- [134] J. P. Estrera, K.T. Passmore. US Patent #5,610,78. (1997).

- [135] R. Li, L. Du, F. Tang, Y. Jiang, Z. Wu, *Appl. Optic.* 55 (2016) 10211.
- [136] L. Du, Z. Wu, Y. Shi, S. Li, Y. Jiang, *Appl. Phys. B* 123 (2017) 283.
- [137] F. Tang, Z. Wu, L. Du, R. Li, Y. Jiang, *J. Mater. Sci. Mater. Electron.* 28 (2017) 4083.
- [138] S. Hu, P. Han, S. Wang, X. Mao, X. Li, L. Gao, *Phys. Status Solidi A* 209 (2012) 2521.
- [139] C.-H. Li, J.-H. Zhao, Q.-D. Chen, J. Feng, H.-B. Sun, *Opt. Lett.* 43 (2018) 1710.
- [140] T. Sarnet, M. Halbwax, R. Torres, P. Delaporte, M. Sentis, S. Martinuzzi, V. Vervisch, F. Torregrosa, H. Etienne, L. Roux, S. Bastide, *Proc. SPIE* 6881 (2008) 688119.
- [141] A. Cavalleri, K. Sokolowski-Tinten, J. Bialkowski, M. Schreiner, D. von der Linde, *J. Appl. Phys.* 85 (1999) 3301.
- [142] J.E. Sipe, J.F. Young, J.S. Preston, H.M. Vandriel, *Phys. Rev. B* 27 (1983) 1141.
- [143] K. Wada, *Proc. SPIE* 5357 (2004) 16.
- [144] J. Xie, K. Huang, X. Yu, Z. Yang, K. Xiao, Y. Qiang, X. Zhu, L. Xu, P. Wang, C. Cui, D. Yang, *ACS Nano* 11 (2017) 9176.
- [145] K. Xu, Y. Chen, T.A. Okhai, L.W. Snyman, *Opt. Mater. Express* 9 (2019) 3985.
- [146] X. Pi, C. Delerue, *Phys. Rev. Lett.* 111 (2013) 177402.
- [147] Y. Chen, D. Xu, K. Xu, N. Zhang, S. Liu, J. Zhao, Q. Luo, L.W. Snyman, *J.W. Swart, Chin. Phys. B* 28 (2019) 107801.
- [148] H. Zeng, W. Cai, Y. Li, J. Hu, P. Liu, *J. Phys. Chem. B* 109 (2005) 18260.
- [149] E. Janzén, R. Stedman, G. Grossmann, H.G. Grimmeiss, *Phys. Rev. B* 29 (1984) 1907.